The local and global geometry of trabecular bone

Callens, Sebastien J.P.; Tourolle né Betts, Duncan C.; Müller, Ralph; Zadpoor, Amir A.

DOI
10.1016/j.actbio.2021.06.013

Publication date
2021

Document Version
Final published version

Published in
Acta Biomaterialia

Acta Biomaterialia 130 (2021) 343–361

Contents lists available at ScienceDirect

Acta Biomaterialia

journal homepage: www.elsevier.com/locate/actbio

Full length article

The local and global geometry of trabecular bone

Sebastien J.P. Callens[a,*], Duncan C. Tourolle né Betts[b], Ralph Müller[b], Amir A. Zadpoor[a]

[a] Department of Biomechanical Engineering, TU Delft, Mekelweg 2, Delft 2628CD, the Netherlands
[b] Institute for Biomechanics, ETH Zurich, Leopold-Ruzicka-Weg 4, Zurich 8093, Switzerland

ARTICLE INFO

Article history:
Received 11 December 2020
Revised 2 June 2021
Accepted 4 June 2021
Available online 12 June 2021

Keywords:
Surface curvature
Minkowski tensors
Morphometry
Trabecular bone
Anisotropy

ABSTRACT

The organization and shape of the microstructural elements of trabecular bone govern its physical properties, are implicated in bone disease, and serve as blueprints for biomaterial design. To devise fundamental structure-property relationships and design truly bone-mimicking biomaterials, it is essential to characterize trabecular bone structure from the perspective of geometry, the mathematical study of shape. Using micro-CT images from 70 donors at five different sites, we analyze the local and global geometry of human trabecular bone in detail, respectively by quantifying surface curvatures and Minkowski functionals. We find that curvature density maps provide distinct and sensitive shape fingerprints for bone from different sites. Contrary to a common assumption, these curvature maps also show that bone morphology does not approximate a minimal surface but exhibits a much more intricate curvature landscape. At the global (or integral) perspective, our Minkowski analysis illustrates that trabecular bone exhibits other types of anisotropy/ellipticity beyond interfacial orientation, and that anisotropy varies substantially within the trabecular structure. Moreover, we show that the Minkowski functionals unify several traditional morphometric indices. Our geometric approach to trabecular morphometry provides a fundamental language of shape that could be useful for bone failure prediction, understanding geometry-driven tissue growth, and the design of bone-mimicking tissue scaffolds.

Statement of significance

The architecture of trabecular bone is key in determining bone properties, and is often a starting point for the design of bone-substitutes. Despite the substantial history of bone morphometry, a fundamental characterization of trabecular bone geometry is still lacking. Therefore, we introduce a robust framework to quantify local and global trabecular bone geometry, which we apply to hundreds of micro-CT scans. Our approach relies on quantifying surface curvatures and Minkowski functionals, which are the most fundamental local and global shape quantifiers. Our results show that these shape metrics are sensitive to differences between bone types and unify traditional metrics within a single mathematical framework. This geometrical framework could also be useful to design bone-mimicking scaffolds and understand geometry-driven tissue growth.

1. Introduction

Many natural and man-made materials are characterized by a complex and often hierarchical spatial architecture. A well-known biological example of such a spatially structured material is trabecular bone, exhibiting a characteristic sponge-like morphology [1]. The quantitative morphological characterization of trabecular bone and other structured materials is essential in the study of these systems, for two primary reasons [2]. First, the morphology or architecture of many materials is often the outcome of a biological or physical process. The study of such morphologies, therefore, provides insight into the mechanisms governing their formation. In trabecular bone, for example, the organization of the microstruc-

* Corresponding author.
E-mail address: s.j.p.callens@tudelft.nl (S.J.P. Callens).

https://doi.org/10.1016/j.actbio.2021.06.013

ture is driven by external loading, and changes in the morphology can be indicative of bone diseases, such as osteoporosis [3–5]. Second, the morphology of spatially complex materials can strongly affect their physical properties, making morphological characterization indispensable for establishing structure-property relationships. For example, this intimate structure-property connection is what enables foams and metamaterials to attain their unique properties [6]. Moreover, material morphology can also directly elicit biological responses in biomaterials, affecting aspects such as cell migration, cell fate and spatial tissue organization [7–10].

In the context of trabecular bone, the importance of the microarchitecture has long been recognized, and many morphometric indices have been proposed [11]. However, such indices typically only quantify a particular morphological aspect, such as density, thickness, or interfacial anisotropy, and often lack a fundamental geometric foundation or interpretation [12]. For example, the well-known structure model index (SMI), which classifies trabecular bone by its rod-like or plate-like nature [13,14], is known to be conceptually flawed by its inability to capture all types of naturally-occurring shapes within the trabecular structure [13,14]. Moreover, calculating the same metric using different software tools often provides significantly different results, owing to substantial variations in the algorithm implementations [15,16]. Hence, there is a need for a unifying, robust approach to quantitatively characterize the shape of complex materials, including trabecular bone. Such a well-defined, mathematical framework is established in the realms of differential and integral geometry, providing fundamental descriptors of local and global shape. Local shape can be accurately captured using the concept of surface curvature. For any small neighborhood on a surface, the mean and Gaussian curvatures, defined in terms of the principal curvatures, capture the most fundamental shape information (Fig. 1). The magnitudes and signs of these measures characterize the local convexity/concavity or the sphere-like *vs.* saddle-like character of the surface. Global shape, on the other hand, can be characterized by the so-called Minkowski functionals (MF). MF are versatile shape indices with strong roots in integral geometry, capable of robustly quantifying different aspects of spatial structure [2,17,18] (Fig. 1). These shape indices, which can be of scalar or tensorial nature, are fundamental in the sense that they form a basis for any other additive functional that describes the shape of a 3D body (Hadwiger-Alesker theorems) [19–21].

These mathematically defined shape metrics have been used to quantify the structure of complex, inanimate materials, such as blends undergoing spinodal decomposition [22] or granular packings [17], but have not yet been used to characterize trabecular bone. Here, we applied these local and global shape measures to hundreds of micro-computed tomography (micro-CT) scans obtained from bone biopsies of 70 donors at five anatomical sites [5]. At the local level, we computed the mean, Gaussian and net curvatures of the trabecular bone interfaces. We observed that the spatial curvature distributions are sensitive to differences in bone microarchitecture from different sites. At the global level, we computed the scalar and tensorial MF, and compared them with traditional morphometric indices. We focused on the more potent tensorial MF that can sensitively quantify the various types of intrinsic anisotropy, which is highly relevant in the study of trabecular bone [23,24]. By using these fundamental shape descriptors, and reconciling them with previous metrics, we provide a novel geometric perspective on trabecular morphometry, that is also compatible with virtually every other type of complex microstructure, including tissue engineering scaffolds and architected biomaterials. As such, our approach does not only offer new insights into trabecular morphology, but also provides a more unified “language of shape” that is useful in the design of bone-mimicking biomaterials [25].

2. Materials & methods

2.1. Trabecular bone data set

All analyses were performed using previously-published, high-resolution μCT data from the European Union BIOMED I Concerted Action “Assessment of Bone Quality in Osteoporosis”. The details of the database composition and data acquisition protocols can be found elsewhere [5,57]. Briefly, the data set comprised trabecular bone biopsies harvested from 70 donors (38 male, 32 female, age between 23 and 92 years) at five anatomical sites: the femoral head (FH), the iliac crest (IC), the calcaneus (CA), the second lumbar vertebra (L2), and the fourth lumbar vertebra (L4). The specimens were scanned using a high-resolution μCT system (μCT 20, Scanco Medical AG, Switzerland) with a spatial resolution of 28 μm and cubic voxels with 14 μm length (for the CA samples, cubic voxels with an edge length of 28 μm were used). A 4 mm^3 cubic volume of interest (VOI) was selected from the resulting scanned data, and 3D binary images of the mineralized bone phase were obtained after Gaussian filtering and thresholding. These binary images served as the basis for all consecutive analyses.

2.2. Surface reconstruction

The binary volume data was processed using custom Python codes and Python-based mesh processing libraries [58,59]. First, a triangle mesh of the trabecular bone surface was reconstructed from the volume data using a marching cubes algorithm with a spacing equal to the voxel size (Supplementary Fig. 7a) [60]. No padding was applied to the volume data prior to the marching cubes algorithm, ensuring that only the trabecular interface was meshed and resulting in a mesh that was a 2-manifold with boundary (Supplementary Fig. 7c). Next, degenerate (zero-area) faces and small disconnected components were removed from the mesh. To account for the roughness inherent in marching cubes meshes, the triangle meshes were smoothed using implicit fairing. This is an efficient smoothing approach that is based on the implicit integration of a diffusion process, and guarantees volume preservation during smoothing [61]. The algorithm solves the linear system:

$$(I - \lambda dtL)M^{n+1} = M^n$$

where M^n represents the set of mesh vertices at iteration n, L represents the Laplacian, and λdt is a user-defined smoothing constant. The trabecular bone meshes were all smoothed using a single iteration and $\lambda dt = 5$, enabling the smoothing of the marching cubes artefacts while maintaining small curved features on the trabecular bone surfaces.

2.3. Curvature estimation algorithm

The principal curvatures of the trabecular bone surface were estimated at every vertex of the discrete triangle mesh using an efficient multiscale fitting algorithm [58,62]. The applied algorithm was an adaption of the Osculating Jets method [63], and fitted a second-order polynomial to a local neighborhood around every vertex for the curvature estimation. The local neighborhood was defined as a ball with a user-defined radius, which was centered at the vertex of interest. For the FH, IC, L2, and L4 trabecular bone meshes, the radius was defined as:

$$r = 10\langle e \rangle$$

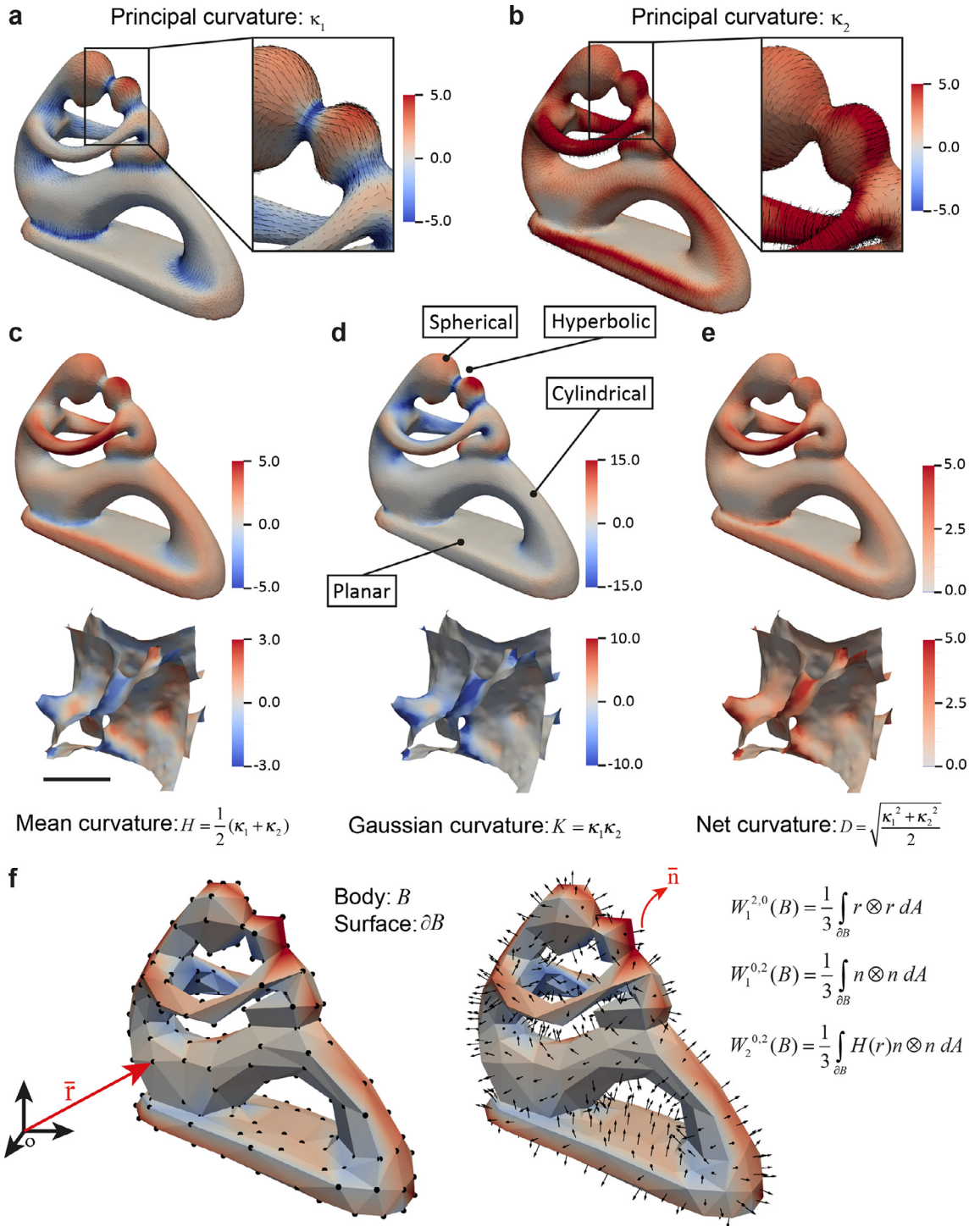

Fig. 1. Surface curvature and Minkowski tensors. (a–b) The minimum (κ_1) and maximum (κ_2) principal curvatures and the associated principal directions on the mesh of a "mother and child" sculpture (model is provided courtesy of UU by the AIM@SHAPE-VISIONAIR Shape Repository). (c–e) The definitions of the mean (H), Gaussian (K), and net (D) curvatures as functions of the principal curvatures. The top row visualizes the curvatures of the "mother and child" sculpture, while the bottom row depicts some small sections of a trabecular bone interface. Spherical, hyperbolic, cylindrical, and planar regions are highlighted in d). The scale bar in c) represents 0.5 mm. (f) A visualization of the components used in the computation of the Minkowski tensors of a coarse "mother and child" model, showing the position vectors ($\bar{r}$) and normal vectors ($\bar{n}$), as well as the expressions for the tensors considered in this study.

where $\langle e \rangle$ represents the average mesh edge length for a particular bone specimen ($\langle e \rangle \approx 20\ \mu\text{m}$). In the case of the CA meshes, which were scanned with a larger voxel size, the radius was set to $r = 5\langle e \rangle$, corresponding to a similarly-sized neighborhood as compared to the other bone specimens. The sensitivity of the curvature estimation algorithm to the neighborhood size (r) and smoothing parameter (λdt) was assessed by calculating the interface shape distributions for a representative sample at different combinations of r and λdt, and by visualizing color-coded curvature distributions on the triangle meshes (Supplementary Figs. 8 and 9).

2.4. Curvature probability density distributions

All reported curvatures were non-dimensionalized using a characteristic length parameter [32]:

$$S_v = \frac{S}{V}$$

where S is the total mesh area and $V = 4^3 mm^3$ is the volume of the cubic specimen. Face curvature values were calculated by averaging the curvatures of the three vertices associated with every face. In constructing the probability density distributions of curvature, the face curvatures were weighted by their face area. In case of the interface shape distributions (ISD), this implied that the ratio of the face areas with a certain combination of curvature to the total mesh area was considered. For example, in case of the ISD of the principal curvature, this means [28]:

$$P_{ISD}(\kappa_1, \kappa_2) = \frac{A(\kappa_1, \kappa_2)}{A_{Total}}$$

2.5. Radial distribution function of curvature

To compute the radial distribution functions (RDF) of the mean and Gaussian curvatures, the curvature values in the range of the 0.5 percentile and the 99.5 percentile were considered. These curvature values were binned in 100 bins of equal width and were weighted by their face areas. Since the RDF considers the curvatures of face pairs separated by a given distance, a characteristic distance was defined in function of the previously described characteristic length scale S_v:

$$r = \tilde{r} S_v^{-1}$$

where $\tilde{\boldsymbol{r}}$ is a user-defined length parameter. In order to find face pairs, a spherical shell of nominal radius r and thickness Δr was centered around the barycenter of every sample face of interest, where:

$$\Delta r = \frac{1}{10} S_v^{-1}$$

All faces with barycenters inside the spherical shell were considered as paired faces to the sampled face. For every bin, 1000 unique random faces were selected and the curvatures of the corresponding paired faces were computed and stored in area-weighted histograms with 100 bins of equal width. If the bin contained less than 1000 faces, which could occur at the extreme values of the curvature range, all available faces were used as sample points in the RDF. By sampling every bin, and combining the corresponding area-weighted curvature histograms of the paired faces, the RDF was constructed as a 100 $\times$ 100 matrix with probability values.

2.6. Minkowski structure metrics

The Minkowski functionals (scalars W_v, tensors $W_v^{r,s}$) and the rotational invariants of the irreducible Minkowski tensors (IMT) (q_s and w_s) were computed on the trabecular triangle meshes using a C++ code (https://github.com/morphometry/karambola) that iterates over all faces, edges, or vertices to compute the relevant Minkowski metrics, in accordance with Table 2 of Ref. [20]. In order to prepare the trabecular bone meshes for the Minkowski metric computation, the non-manifold edges and vertices that could result after the marching cubes reconstruction had to be removed. The non-manifold edges were removed by constructing the face adjacency matrix of the mesh and removing those faces with edges shared by more than two faces. Non-manifold vertices that remained after the deletion of non-manifold edges were removed using Meshlab [64]. Of the six relevant Minkowski tensors, only the tensors $W_1^{0,2}$ and $W_2^{0,2}$ are translation-invariant tensors, which means that:

$$W_v^{r,s}(B \uplus t) = W_v^{r,s}(B)$$

where $B \uplus t$ signifies the translation of body B along vector t [20]. The other Minkowski tensors are translation-covariant, and do not satisfy this relationship. For those translation-covariant tensors, a consistent definition of the mesh origin is required to enable a fair comparison between the different meshes. For all the trabecular bone meshes, the origin was defined to be in the center of the cubic bounding box.

In order to deal with the open trabecular bone meshes, a domain-wise analysis of the Minkowski metrics was performed. To this end, the faces at the boundaries of the mesh were assigned a different label than the faces inside the trabecular surface, and the Minkowski metrics were computed for each labeled domain separately. In this way, the faces not on the boundary are effectively considered to be part of a "closed" surface, and all the relevant Minkowski metrics could be calculated, which is not the case for the "open" boundary faces [20]. Representing a mesh as a doubly-connected edge list (DCEL), the boundary faces are those faces with at least one half-edge that appears only once in list (*i.e.*, it is not shared with another face). A visual representation of the boundary face labeling is provided in Supplementary Fig. 10a.

2.7. Spatial decomposition

A domain-wise Minkowski analysis was performed on spatially decomposed meshes. The mesh was subdivided into a 3 $\times$ 3 $\times$ 3 cubic grid, and all faces were assigned a label based on the location in the grid, resulting in a total of 28 different labels (27 labels for the grid domains and one label for the boundary, see Supplementary Fig. 10b). The relative difference between the local and global DA was defined as:

$$\tilde{\lambda}_v^{r,s} = \frac{\frac{\left|\lambda_v^{r,s}\right|_{min}}{\left|\lambda_v^{r,s}\right|_{max}} - \left\langle \frac{\left|\lambda_v^{r,s}\right|_{min}}{\left|\lambda_v^{r,s}\right|_{max}} \right\rangle}{\left\langle \frac{\left|\lambda_v^{r,s}\right|_{min}}{\left|\lambda_v^{r,s}\right|_{max}} \right\rangle}$$

Here, $\frac{|\lambda_v^{r,s}|_{min}}{|\lambda_v^{r,s}|_{max}}$ defines the ratio of the minimal to the maximal eigenvalue of the tensor $W_v^{r,s}$, while $\langle\cdot\rangle$ refers to the average value.

For the calculation of the quadratic and cubic invariants of the irreducible Minkowski tensors (IMT), the rank s was in the range of $[0, 8]$.

2.8. Ellipsoid representation of tensors

The rank-2 Minkowski and MIL tensors were visualized by ellipsoid surfaces, with radii and directions that were defined by the eigenvalues and eigenvectors of the tensors, respectively [38,41]. The surface of an arbitrarily oriented ellipsoid, centered at the origin is obtained by solving the following expression for x:

$$x^T M x = 1$$

where M is a positive-definite matrix. The eigenvalues λ_s of M are related to the semi-axes c_s of the ellipsoid by:

$$\lambda_s = \frac{1}{c_s^2}$$

The corresponding eigenvectors then represent the principal orientations of the ellipsoid. By exploiting this relationship, the eigenvalues and eigenvectors of the rank-2 tensors used in this work could be represented as ellipsoid surfaces. In visualizing the ellipsoids of the spatially decomposed samples, the ellipsoids were uniformly scaled to the same volume, which is given by:

$$V = \frac{4}{3}\pi c_1 c_2 c_3$$

2.9. Standard bone morphometric analyses

The mean intercept length (MIL) analysis was performed by applying the algorithms implemented in BoneJ (version BoneJ2), which is an ImageJ plug-in, to the binary image stacks of the trabecular specimens [42]. While the earlier implementations of the MIL could suffer from significant deviations in the predicted anisotropy due to sampling bias [38,43], the current implementation draws test lines through the entire image stack, offering a more uniform sampling. A convergence analysis was performed to assess the influence of the number of the parallel test lines and the number of different test line directions. For the final analyses, 2000 directions and 10000 lines per direction were used. Moreover, the MIL results for every sample were taken as the average of three runs of the MIL algorithm. The Euler characteristic (χ) was also estimated using BoneJ, on the same binary image data as was used for the MIL analysis. Since the estimation of the Euler characteristic assumes a single connected component, the images were purified (using the Purify command in BoneJ) prior to the connectivity computation. The other reported morphometric indices (*i.e.*, BS and $\partial S/\partial r$) were obtained from the Scanco micro-CT scanner software (Scanco Medical AG, Switzerland).

2.10. Statistical analysis

The Kruskal-Wallis H test was used to detect significant differences between the means of the different groups of data. *Post hoc* comparisons of the means were performed using the two-sided Mann-Whitney U tests. The two-sample Kolmogorov-Smirnov test was used to assess the differences between the probability distributions of the q_s and w_s metrics, and the age-related curvature probability distributions. The obtained results were considered to be statistically significant when $p < 0.01$. All statistical analyses were performed using the python library Scipy.

3. Results

3.1. Surface curvature of the trabecular bone interface

We started our geometric analysis at the most local scale, by estimating the mean (H), Gaussian (K), and net (D) curvatures of the trabecular bone interfaces from their triangulated mesh representations. The mean curvature describes how much a surface is locally convex or concave. The Gaussian curvature quantifies the type of the surface: $K < 0$ signifies a saddle-shaped region (hyperbolic), $K = 0$ implies an intrinsically flat region (such as a plane, cylinder or cone), and $K > 0$ describes a sphere-shaped region (Fig. 1). The net curvature is less common and describes how much a surface locally deviates from a planar region (Fig. 1).

Fig. 2 depicts the mesh representations of three representative trabecular bone specimens from the femoral head (FH), iliac crest (IC), and second lumbar vertebra (L2), color-coded by their curvature (representative visualizations of the calcaneus (CA) and fourth lumbar vertebra (L4) are provided in Supplementary Fig. 1). The FH samples typically exhibited an apparently uniform dispersion of regions with positive and negative values of the mean curvature. Comparing this to the L2 specimen, we observed that the latter showed much more regions of highly negative mean curvature. This is the consequence of the many rod-like elements that are typically present in specimens from the lumber spine, as opposed to the more sheet-like architecture in FH specimens [5]. The Gaussian curvature distributions clearly showed that the geometry of trabecular bone is, on average, hyperbolic in nature ($K < 0$). This has been reported before for a few bone biopsies [26]. This prevalence of negative Gaussian curvature is consistent with the high topological complexity (*i.e.*, high genus) of trabecular bone, according to the Gauss-Bonnet theorem [27]. The net curvature captures regions where the trabecular surface is strongly bent, without distinguishing between the saddle- or sphere-like nature of these bends. In FH specimens, such regions corresponded primarily to arc-like transitions between plate-like elements, while high net curvature in IC or L2 specimens was concentrated in the cylindrically-shaped rod-like elements.

As described before, trabecular bone has often been characterized on the basis of its plate-like or rod-like nature, and the SMI was developed to quantify this nature. To relate this characterization to our curvature analysis, we estimated the curvatures of idealized rod, plate, and mixed plate-rod lattices of $3 \times 3 \times 3$ unit cells. Visualizing the curvatures reveals that these idealized lattices exhibit a much narrower curvature spectrum than typical trabecular bone specimens, irrespective of the anatomical site (Fig. 2d–f). In particular, the Gaussian curvature spectrum is very limited, since both the cylindrical rods and the plates have $K = 0$. For these idealized lattices, non-zero Gaussian curvature only appears at the rod-rod, rod-plate and plate-plate intersections. These curvature visualizations indicate that the plate *vs.* rod paradigm, though relevant for general discussions, only provides a limited ability to characterize the local shape variations that are present in trabecular bone.

3.2. Curvature distributions

Due to the inherently local nature of surface curvature, the average values of curvature are not of much descriptive use. In fact, the average mean and Gaussian curvatures are already captured in the structure model index (SMI$\sim \langle H \rangle$) and Euler-Poincaré characteristic ($\chi \sim \langle K \rangle$), respectively [26]. Instead, it is important to consider the distribution of curvature throughout the trabecular specimens. Therefore, we computed the 1D and 2D probability distributions of the different curvature measures, obtained from more than 60 subjects at every anatomical location. The 1D probability densities of the mean curvature (Fig. 3) confirmed the above-mentioned observation that predominantly plate-like specimens (*i.e.*, FH) exhibit a more uniform distribution of the normalized mean curvature, with a peak close to $H/S_v \approx 0$, than predominantly rod-like specimens (*i.e.*, L2 and L4). The latter displayed a flattened and more negatively skewed distribution, centered around $H/S_v \approx -0.5$. The mean curvature density also reflected the intermediate nature of the iliac crest (IC) and calcaneus (CA) specimens, containing both plate-like and rod-like elements. As expected, the Gaussian curvature density functions were negatively skewed, with a sharp peak around $K/S_v^2 \approx 0$.

Since a full description of surface curvature is typically built on two variables, such as the pair of principal curvatures, we quantified the interface shape distributions (ISD) for different curvature measures. These types of 2D probability density maps have been used to characterize the morphological evolution of spinodal decomposition systems during coarsening [28,29]. The ISD of the principal curvatures provides a density map of all possible shapes that could be encountered on the trabecular surface, such as planar cylindrical, spherical, or saddle shapes (Fig. 4a). The horizontal axes contain all purely cylindrical shapes, and the upper left quadrant contains all saddle shapes. The predominantly convex saddles (*i.e.*, where $|\kappa_1| > |\kappa_2|$) are situated below the diagonal dotted line, while the predominantly convex saddles are situated above. The demarcation line between those saddles contains the so-called minimal surfaces, where $\kappa_1 = -\kappa_2$. While the ISD of the principal curvatures captures all the possible shapes, the SMI was originally defined for predominantly convex shapes, excluding a substantial portion of the curvature spectrum (Fig. 4b). We plotted the ISD of the principal curvatures, as well as the ISD of the net (D) *vs.* mean (H) curvatures for the idealized rod structure that was in-

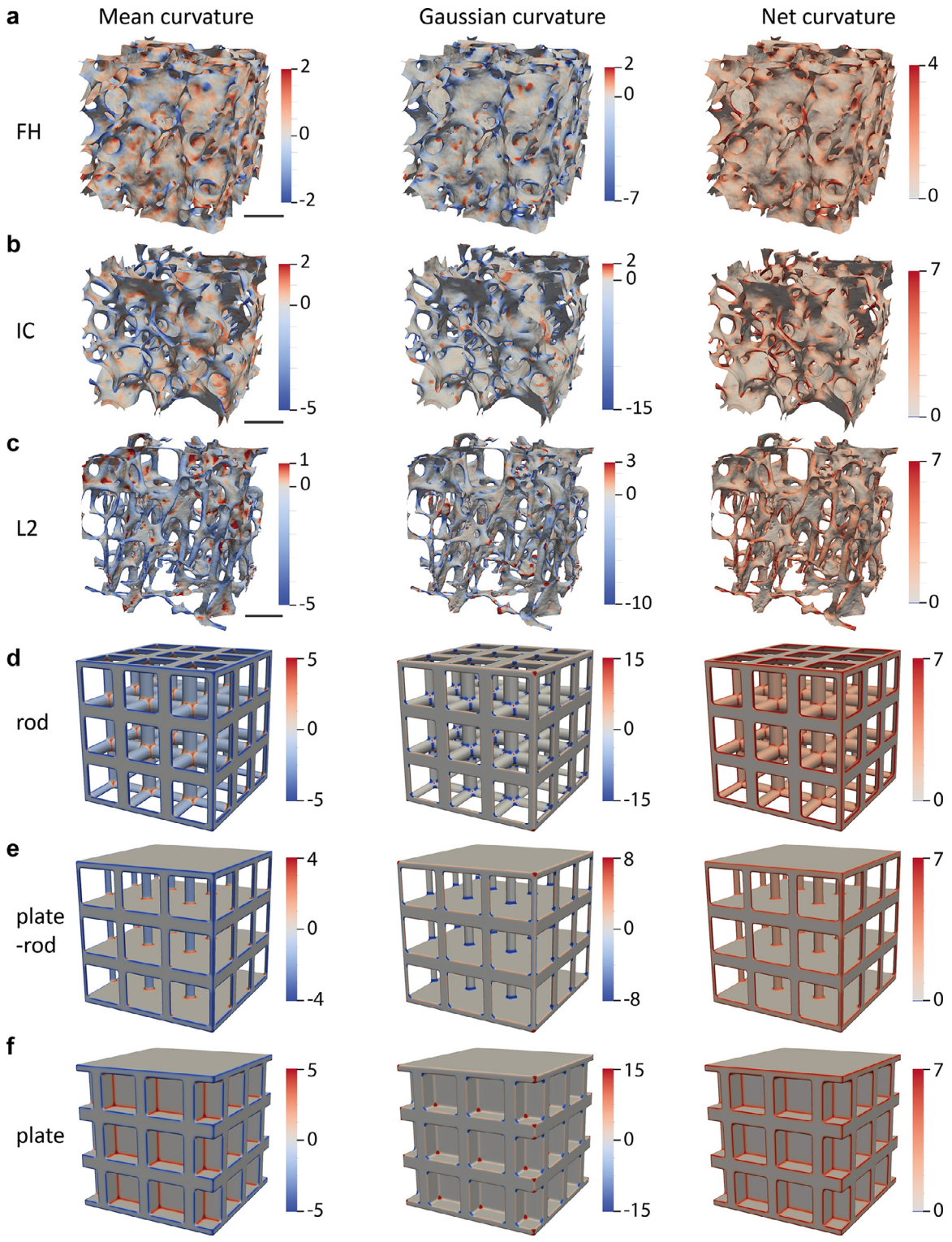

Fig. 2. Curvature estimation on triangle meshes. (a–c) The normalized mean, Gaussian, and net curvature visualizations of some representative (regarding morphology) trabecular samples from the femoral head (FH) the iliac crest (IC) the second lumbar vertebra (L2). The scale bars represent 1 mm. (d–f) The same curvature visualizations for idealized rod, plate-rod and plate structures (3 × 3 × 3 lattices), respectively.

troduced earlier (Fig. 4c–d). These curvature density maps confirm that the idealized rod structure exhibits a very narrow curvature spectrum, with the primary peak in Fig. 4c and 4d corresponding to the curvature of the cylindrical rods. In the case of the plate and plate-rod structures (data not shown), this spectrum would be even narrower, with most data points located at the origin.

Next, we computed the ISD of the principal curvatures, the ISD of the net *vs.* mean curvature, and the ISD of the Gaussian *vs.* mean curvature for all the bone meshes, grouped by anatomical site (Fig. 5). For example, the principal curvature ISD of the FH specimens showed that most of the interface corresponds to saddle-shaped regions, and that sphere-like indentations (top right quad-

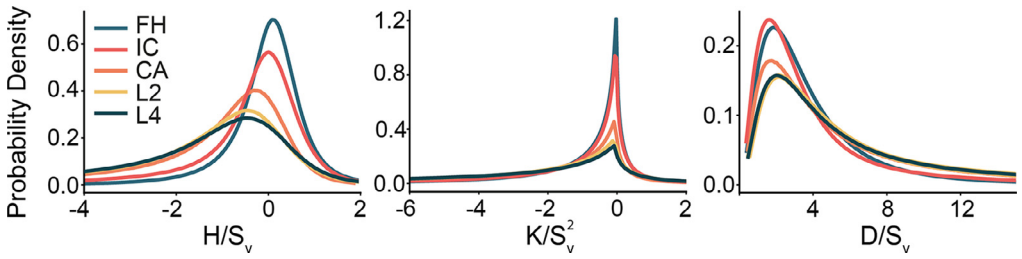

Fig. 3. 1D curvature distributions. (a) Probability density distribution of the normalized mean (left), Gaussian (middle) and net (right) curvature per bone type. Each curve contains data from several samples ($n_{CA} = 66, n_{FH} = 62, n_{IC} = 68, n_{L2} = 65, n_{L4} = 68$).

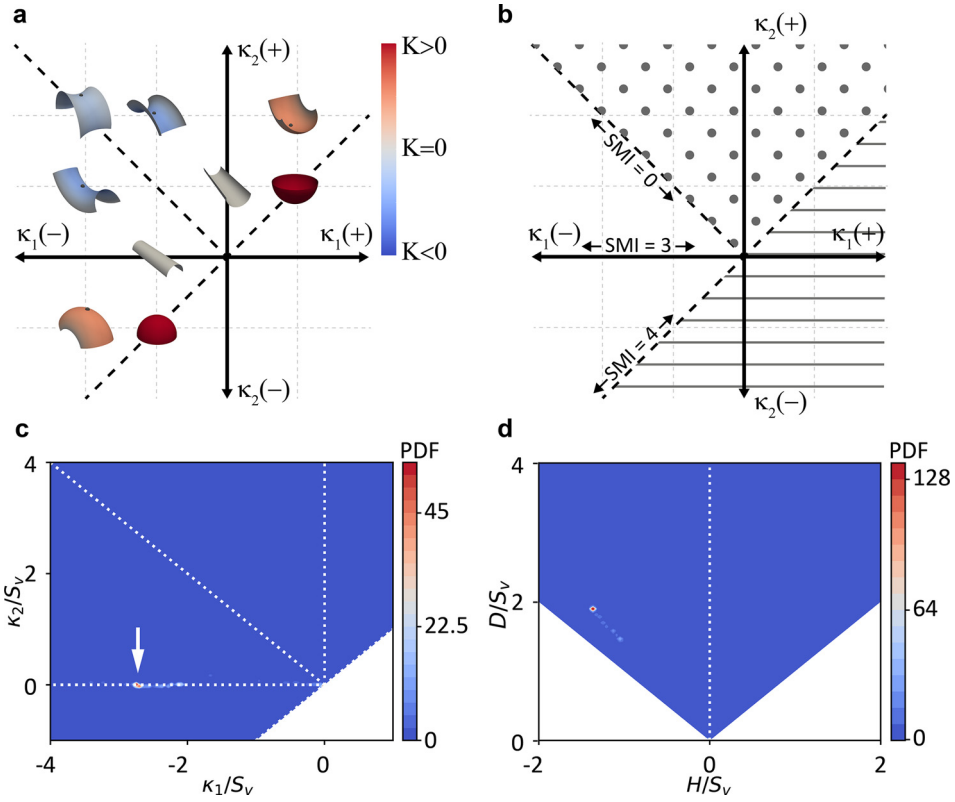

Fig. 4. Interpretation of the interface shape distributions. (a) A schematic drawing outlining the localization of various curved shapes on the 2D curvature distribution plot that is referred to as the interface shape distribution (ISD). The shapes are colored by their Gaussian curvature *K*. (b) The relation between the ISD of principal curvatures and the SMI. The horizontally hatched region is theoretically unfeasible ($\kappa_1 > \kappa_2$). The dotted region contains shapes that are on average concave, while the SMI was originally defined for convex shapes. (c–d) The normalized ISD of principal curvatures and of the net *vs.* mean curvatures respectively, for the idealized rod structure of Fig. 2d.

rant), and not protrusions (bottom left quadrant), were the primary source of positive Gaussian curvature in these specimens. The ISD of the principal curvatures captured the progressive transition from primarily plate-like to primarily rod-like bone specimens (Fig. 5). While the FH specimens exhibited a relatively concentrated, circular distribution of curvatures, the rod-like specimens of L2 and L4 were characterized by a much broader distribution with a horizontal orientation. These rod-like elements were not perfect cylinders, however, but were slightly saddle-shaped. The IC samples exhibited a principal curvature distribution that was similar to that of the FH, indicating primarily plate-like elements. For the CA samples, a horizontal orientation of the distribution was apparent, indicating a higher proportion of rod-like elements in the structures. The morphological differences between bone types were also observed in the joint probability distributions of the normalized net (D/S_v) and mean curvature (H/S_v), and the transition from plate-like to rod-like specimens was clearly visible (Fig. 3). Moreover, these distributions again showed that the mean curvature of trabecular bone is, in general, not uniformly centered around zero. For our FH specimens, the peak of the mean curvature was situated slightly above $H = 0$, indicating shapes that were more concave than they were convex. This peak transitioned towards negative values for rod-like specimens, due to the convex nature of the rods. The ISD of the mean and Gaussian curvatures also captured this distinction between the different bone types, again showing a broader distribution for more rod-like specimens. Taken together, these curvature density maps confirm that the trabecular bone exhibits a broad curvature spectrum, much broader than that of idealized rod or plate structures, and that all types of local shapes can be found on the trabecular interface, although the majority is of a hyperbolic nature. Additionally, the plots confirm that the shape of the curvature distributions can act as a fingerprint for the type of the bone (anatomical site), and that these plots are sensitive to gradual changes in the bone shape, as opposed to the binary classification of rod-like *vs.* plate-like.

In an effort to explore the potential effects of age on the curvature distributions and, thus, the local shape changes, we plotted the various normalized ISDs for the FH and L4 specimens from

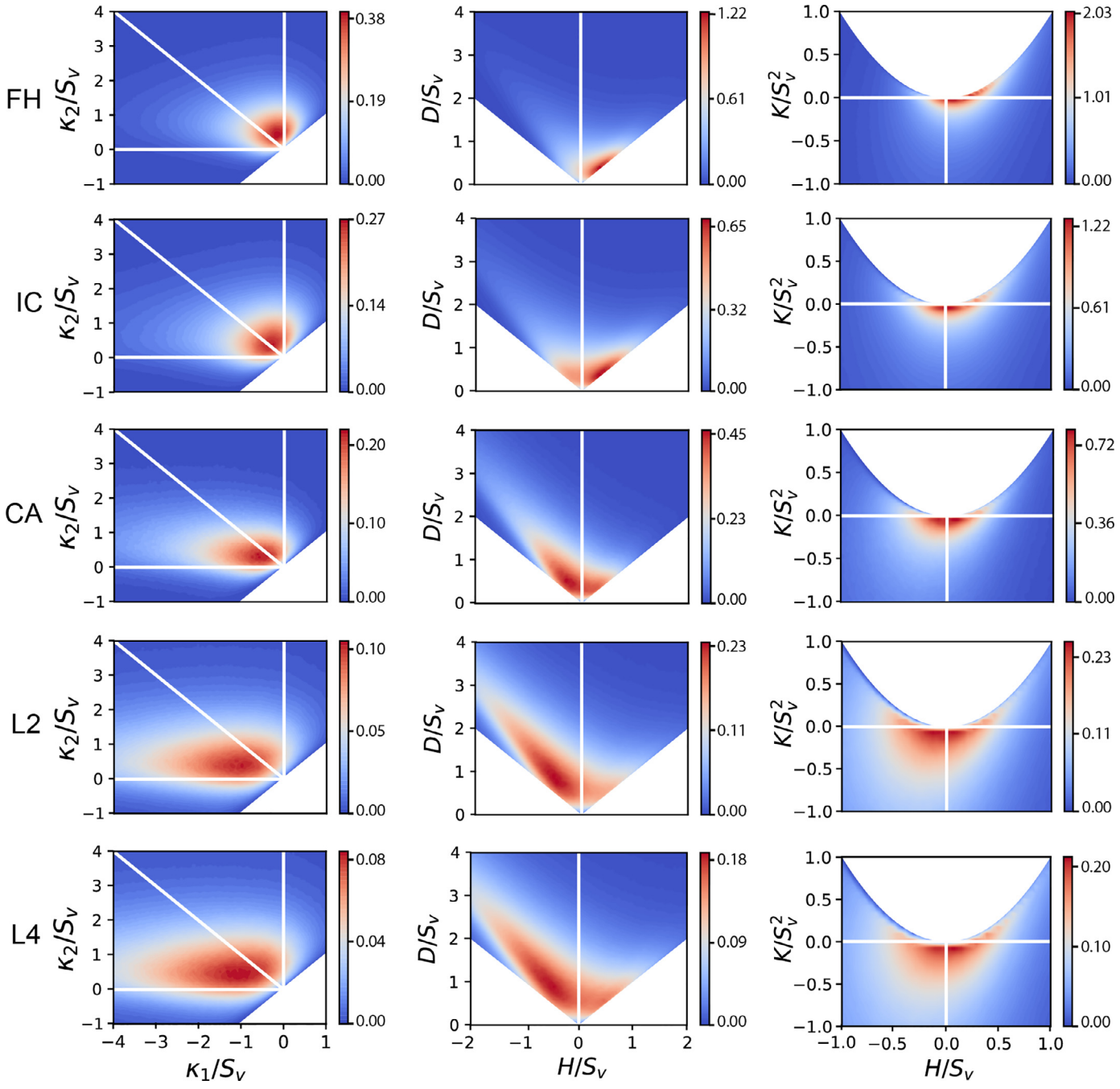

Fig. 5. 2D curvature distributions of trabecular bone. The interface shape distributions (ISD) for specimens from every anatomical site, showing the normalized curvature probability densities. Left column displays the ISD of the principal curvatures (κ_1 and κ_2). Middle column displays the ISD of the net (D) and mean (H) curvatures. Right column displays the ISD of the Gaussian (K) and mean (H) curvatures. Each plot contains data from several specimens ($n_{CA} = 66$, $n_{FH} = 62$, $n_{IC} = 68$, $n_{L2} = 65$, $n_{L4} = 68$).

different age groups. Specifically, we included 15 specimens from the donors younger than 60 and 15 specimens from the donors older than 80 (Fig. 6), and we kept the color bars constant for both age groups. Considering the FH specimens, we did not observe substantial changes in the shape and magnitudes of the curvature density plots between both age groups (Fig. 6a–b). For the L4 specimens, however, the ISD plots of the donors older than 80 showed a much broader curvature density distribution than those of the donors younger than 60, implying that the curvatures are spread out more, and that locally higher curvatures are reached throughout the specimens (note that these plots represent probability densities and should all integrate to 1).

The age-dependent changes in the ISDs of the L4 specimens are in line with the earlier observations indicating that the trabecular bone in the vertebrae is more prone to noticeable structural changes with advancing age, as opposed to the bone from the FH [30]. Local analyses of the trabecular elements revealed that rod-like elements in the vertebrae progressively thin and eventually vanish, leaving only thicker rods. Additionally, plate-like elements become perforated, and eventually transition into rod-like elements [30]. The thinning, splitting, and perforating adaptations would result in local curvature concentrations (Fig. 7), hence contributing to the more spread-out curvature distributions in the ISDs. Moreover, individual variations in trabecular bone morphology are known to increase with age, leading to larger variations

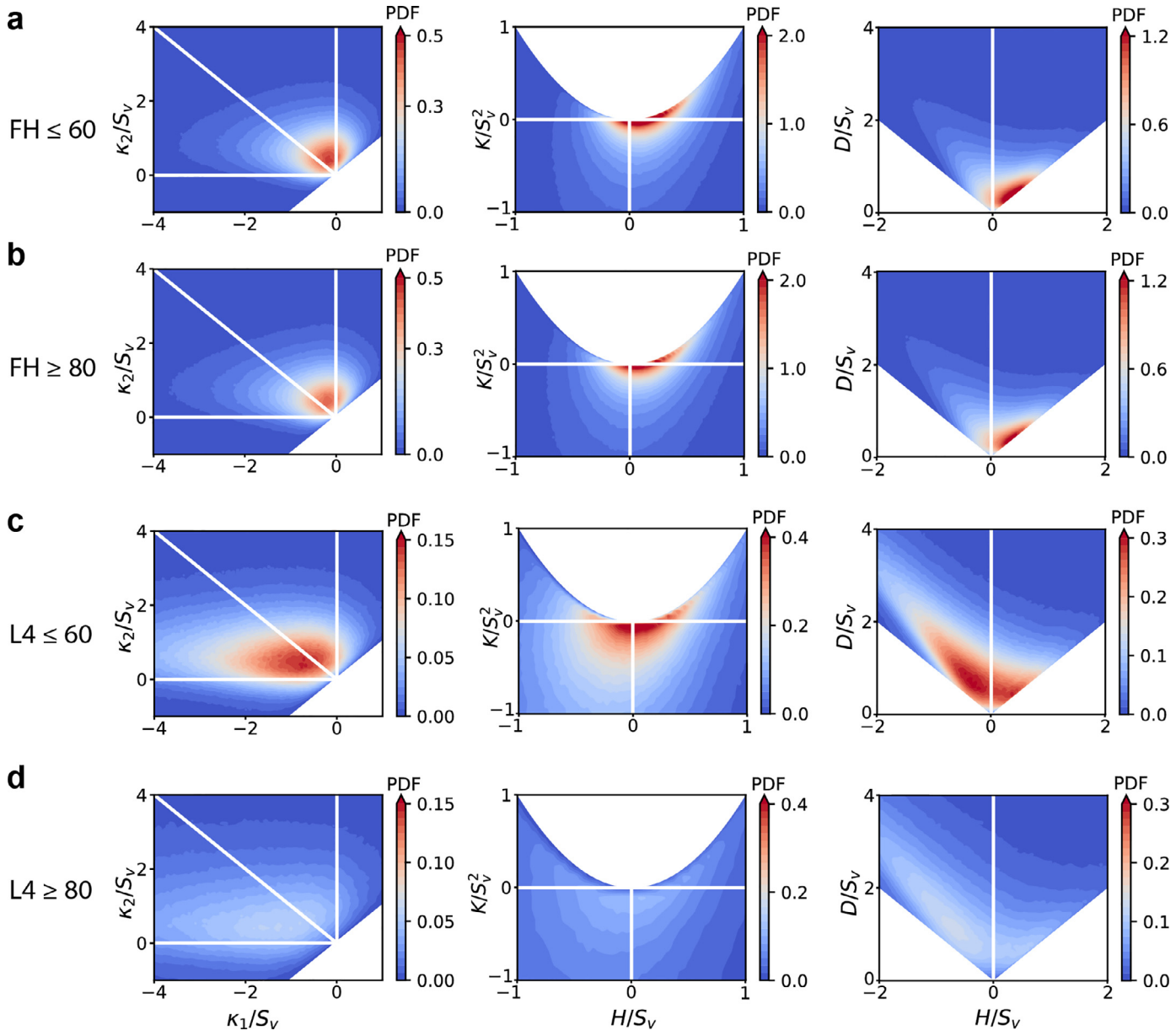

Fig. 6. The effect of age on the 2D curvature distributions. The left column displays the normalized ISD of the principal curvatures (κ_1 and κ_2). The middle column displays the normalized ISD of the net (D) and mean (H) curvatures. The right column displays the normalized ISD of the Gaussian (K) and mean (H) curvatures. Every plot contains the data from 15 specimens. (a–b) Specimens from the femoral head from donors ≤ 60 years old and ≥ 80 years old, respectively. (c–d) The specimens from the fourth lumbar vertebra from donors ≤ 60 years old and ≥ 80 years old, respectively.

in curvature distribution and rendering it challenging to detect age-related bone changes with these metrics alone. An important note regarding these ISDs is that the curvatures are normalized using the characteristic length, which is based on the bone surface area, which is also affected by age. Hence, these results should be interpreted as area-normalized curvature changes with advancing age. Non-normalized 1D curvature probability distributions are provided in Supplementary Fig. 2, and also confirm that the most noticeable curvature change with age are observed in the trabecular bone from the vertebrae.

3.3. Radial distribution function

The ISD characterizes the local shape of trabecular bone by providing insight into the range and frequencies of the different types of curvature. However, it does not provide information about the way these curvatures are distributed in space and how the curvatures at different locations in the structure are related. Knowledge of this spatial correlation is relevant, since two structures could (theoretically) exhibit the same ISD, while having their curvatures distributed differently throughout space [22]. Therefore, we quantified the spatial correlation of the mean and Gaussian curvatures, using a curvature-based radial distribution function (RDF). Traditionally, the RDF has been employed in the analysis of granular systems, where it quantifies the likelihood of finding particles at a certain distance from a reference particle, relative to what would be expected based on the overall density of the system [31]. Depending on the type of the particle system and the associated interactions, the (excess) probability of finding neighboring particles will vary as a function of distance. The RDF has also gained popularity to quantify the spatial correlation in non-particulate systems [2]. When defined on the basis of the mean curvature, the RDF has

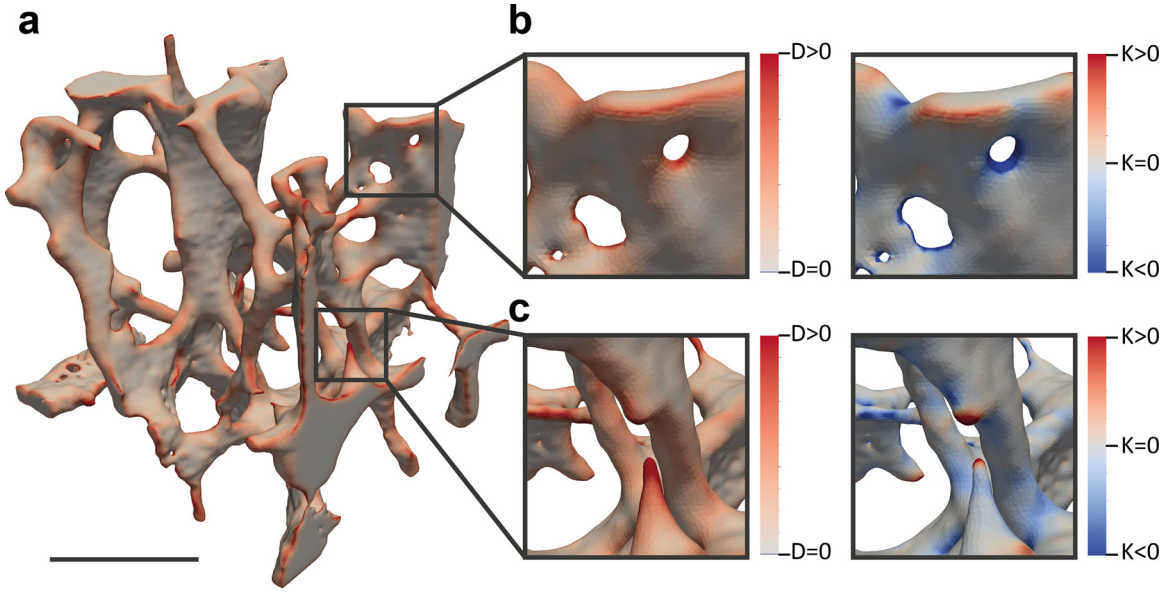

Fig. 7. Expected surface curvature changes during age-related bone adaption. (a) A section of the trabecular bone from the second lumbar vertebra of a 68-year-old female donor, color-coded by net curvature (D). The scale bar represents 1 mm. (b) The close-ups of a plate-like region that shows perforations, resulting in some additional regions of increased net curvature and negative Gaussian curvature. (c) A close-up of the thinning and disappearing rods, resulting in some localized peaks of the positive net and Gaussian curvatures at the end caps.

been used to complement the ISD in characterizing the coarsening dynamics of spinodal decomposition systems [22,32]. In this sense, the RDF provides a slightly more global interpretation of curvature than the ISD. Here, we used a similar approach to compute the RDF of the mean and Gaussian curvature for the trabecular bone specimens from the different anatomical sites. In case of the mean curvature, we define the RDF as:

$$G(H_2|r,H_1) = \frac{A_{H_2,S}(r)/A_S(r)}{A_{H_2,T}/A_T}$$

Here, $A_{H_2,S}(r)$ is the total area of faces with a mean curvature of H_2 within a spherical shell of radius r, centered around a reference point with a mean curvature of H_1. $A_S(r)$ represents the total area of all faces inside the spherical shell, $A_{H_2,T}$ is the total area of faces with the mean curvature H_2 in the entire specimen, and A_T is the total face area of the entire specimen. Hence, $G(H_2|r,H_1)$ describes the area-density of the faces with H_2 at a distance r from a face with H_1, relative to the overall area-density of the faces with H_2. As such, the RDF captures how much more ($G > 1$) or less ($G < 1$) likely it is to find pairs of faces with a certain combination of mean curvature at a given distance from each other as compared to a random distribution throughout the specimen [32].

We plotted the RDF of the normalized mean (Fig. 8) and Gaussian (Supplementary Fig. 3) curvature at several characteristic distances. Taking the mean curvature RDF as the running example, the plots should be symmetric about the line $H_1/S_v = H_2/S_v$, since $G(H_2 r, H_1) = G(H_1|r,H_2)$ [22]. Considering the RDF plots for $\tilde{r} = 0.06$ (left column in Fig. 8), several observations could be made. For example, distinct positive correlations ($G > 1$) and anti-correlations ($G < 1$) were observed in all specimens. The positive correlations increased for the more extreme values of curvature, indicating that those strongly curved regions are highly concentrated in the structure. In other words, points with high mean curvature values are likely to have neighbors with high mean curvature as well. On the other hand, it is less likely to encounter neighbors with curvatures on the opposite sides of the spectrum (anti-correlation). For the FH, IC, and CA samples, a relatively stronger positive correlation was observed along the entire line $H_1 = H_2$ than for the L2 and L4 samples. Additionally, stronger anti-correlations were observed in the FH, IC and CA specimens. It is also noteworthy that the range of curvatures is substantially larger for the rod-like samples (L2 and L4) than for the plate-like samples (FH), indicating that the positive correlations in the rod-like samples occur at more extreme locations (relatively speaking) than for the plate-like samples. At the larger values of $\tilde{r}$ the correlations and anti-correlations gradually dissipated, and the RDF became more uniform and approached $G = 1$. The most extreme values of curvature maintained some positive correlation at $\tilde{r} = 0.14$, for all specimens. However, the correlation dissipation occurred faster in the L2 and L4 specimens, showing a more uniform distribution of G around unity than the FH, IC, and CA samples. The RDF of the Gaussian curvature (Supplementary Fig. 3) exhibited a similar effect, although the positively correlated region had a more triangular shape. Moreover, at small and intermediate distances, high positive correlations were observed for the entire range of the positive Gaussian curvatures, indicating that locally spherical features are highly concentrated in trabecular bone.

The RDF of the surface curvature was originally developed to study the time-dependent evolution, also known as coarsening or Ostwald ripening, of complex bicontinuous morphologies that are observed after the spinodal decomposition of two-phase mixtures [32]. These morphologies undergo coarsening to reduce the overall interfacial energy, through a diffusion-driven process. An analysis of the mean curvature RDF of such spinodal systems for a range of distances r revealed oscillations of the correlations and anti-correlations between curvature pairs with equal or opposite signs. The distance over which this oscillating behavior is observed before it decays was found to be a characteristic length that describes the desired distance between regions of positive and negative mean curvature to obtain the optimum diffusion gradient for coarsening [22,32]. While these spinodal morphologies visually appear similar to trabecular bone, the fast decay of the correlations and the lack of oscillatory behavior in the RDF of the trabecular bone specimens indicate that both types of morphologies are quite different in terms of their spatial distribution of curvatures. Moreover, this implies that the evolution of the trabecular bone morphology follows a different process than that of other, seemingly similar bicontinuous morphologies.

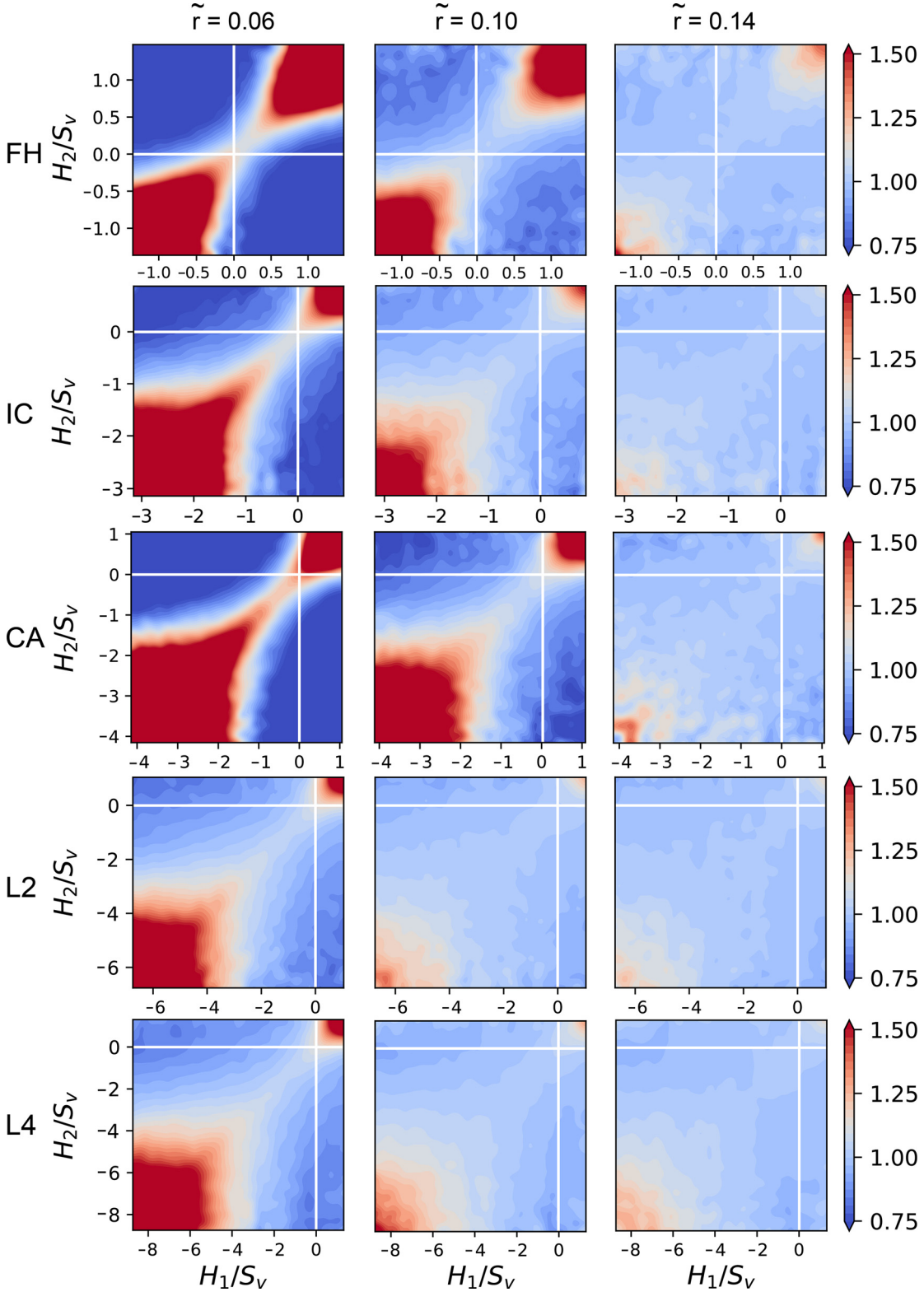

Fig. 8. Radial distribution function. Plots showing the radial distribution function of normalized mean curvature (G) for representative (regarding morphology) specimens from the five anatomical sites, at different values of the characteristic distance $\tilde{r}$. Color bar indicates enhanced ($G > 1$) or reduced ($G < 1$) probability of finding mean curvature pairs ($H_1 - H_2$) at a given distance ($\tilde{r}$) from each other, with respect to randomly distributed curvatures. Left column: $\tilde{r} = 0.06$, middle column: $\tilde{r} = 0.1$, right column: $\tilde{r} = 0.14$.

3.4. Scalar Minkowski functionals

The ISD presents the most local measure of trabecular shape, by characterizing the curvatures at individual points along the interface. Two-point correlation functions, such as the RDF presented above, provide a slightly more global picture by considering pairs of points throughout the structure. Nevertheless, it is useful to complement these approaches with truly global, or integral, metrics that describe the shape as a whole. From an integral geometric viewpoint, the most fundamental indices to characterize the global shape are the Minkowski functionals. Their fundamental nature for shape description is described in Hadwiger's theorem (generalized to tensors by Alesker), stating that any other motion-covariant, conditionally continuous, additive functional on a body is a linear combination of the Minkowski functionals [19–21]. In addition to their fundamental nature, Minkowski shape indices are also highly versatile, meaning that they can be applied to a broad spectrum of complex structures, and are robust against noise [2,20].

The simplest types of Minkowski functionals are of a scalar nature and are further referred to as the Minkowski scalars (see Supplementary Note 1 for the mathematical formulations and background). For a 3D body B (Fig. 1f), four scalar MF can be defined, which are proportional to the volume ($W_0(B)$), the total area of the bounding surface ($W_1(B)$), the area-integrated mean curvature ($W_2(B)$), and the area-integrated Gaussian curvature ($W_3(B)$). The latter is proportional to the Euler-Poincaré index, a topological invariant describing connectivity. The Minkowski scalars have been applied in the analysis of various spatial architectures, including voxelized representations of trabecular bone [33]. Here, we computed the Minkowski scalars W_1, W_2, and W_3 on the smoothed triangle meshes of the trabecular bone interface, and compared them to traditional bone morphometric indices that characterize the global trabecular shape (Fig. 9) [5,12]. The scalar W_0 was omitted, since it is not defined for open surfaces. The scalar W_1 and the bone surface area (BS) were relatively well correlated (Fig. 9a). The strongest correlation was observed for the L4 specimens ($\rho = 0.91$), while the weakest correlation was attained in the CA specimens ($\rho = 0.66$). The deviations between the computed W_1 and BS could potentially be attributed to different underlying meshes (BS was directly calculated on a marching cubes mesh [5]). The scalar W_2, which captures the area-integrated mean curvature, is plotted against the morphometric parameter $\partial S/\partial r$, showing strong correlations for all bone types ($\rho > 0.87$, Fig. 9b). The parameter $\partial S/\partial r$ represents a surface area derivative, and is estimated as the change in surface area (dS) when the surface is dilated by a small amount, divided by the length of that dilation (dr). The area of such a dilated parallel surface (S_r) is related to the area of the original surface (S_0) and its curvature by [26]:

$$S_r = S_0\left(1 + 2\langle H\rangle r + \langle K\rangle r^2\right)$$

where r is the signed distance from the original surface, $\langle H\rangle$ is the area-averaged mean curvature, and $\langle K\rangle$ is the area-averaged Gaussian curvature. The dilation-based parameter $\partial S/\partial r$ appears in two well-known bone morphometric indices: the SMI and the 3D trabecular bone pattern factor (TBPf) [13,34,35]:

$$SMI = 6\frac{BV \cdot \frac{\partial S}{\partial r}}{BS^2}$$

$$TBPf = \frac{\frac{\partial S}{\partial r}}{BS}$$

In that sense, both SMI and TBPf are proportional to the average mean curvature ($\langle H\rangle$) of the surface (for small dilations ($r^2 \approx 0$), the second-order Gaussian curvature contribution can be neglected), essentially meaning that the $\langle H\rangle$ is a global morphometric index [26,30]. Overall, the correlation between W_3 and the Euler-Poincaré index (χ) is lower ($0.42 < \rho < 0.76$) than the correlations between the previous Minkowski scalars and their corresponding morphometric indices (Fig. 9c). This could again be attributed to the different calculation approaches: W_3 is based on the integral Gaussian curvature of the triangle meshes, while χ is computed on 3D binary images. Finally, an important observation is that W_3 captures the differences between the specimens from different anatomical sites, while these are not reflected in the χ values (Fig. 9c). This implies that W_3 could potentially be more sensitive to subtle changes in connectivity than χ (*e.g.,* in case of a disease). Combined, these scalar Minkowski functionals capture the different aspects of global trabecular bone geometry, and unify the traditional metrics within a single framework, using the same data representation and computation approach.

3.5. Tensorial Minkowski functionals

A relatively novel extension of the Minkowski scalars for global shape quantification is provided by the so-called Minkowski tensors (MT). Due to their tensorial nature, these MT capture the orientation-dependent aspects of morphology, a feature that is highly relevant for the study of heterogeneous materials such as trabecular bone [23,24]. While the MT have been employed to characterize granular packings, galaxies, or foams [17,36,37], we are the first to apply these tensors to the study of trabecular bone. As a natural consequence of their mathematical foundation, many different MT can be defined, each characterizing a different aspect of morphology. In principle, the MT can be defined for any arbitrary rank, but we primarily focused on rank-two tensors, due to their intuitive physical interpretation [2]. Higher rank MT are briefly considered in Section 3.7. For a 3D body, six relevant rank-two MT are defined (Fig. 1 and Supplementary Note 1). As an example, the tensor $W_0^{2,0}(B)$ is a measure of the spatial distribution of mass for a solid body B, in some sense analogous to the moment of inertia tensor. The tensor $W_1^{2,0}(B)$, on the other hand, measures the mass distribution when the entire mass of B is homogeneously distributed on the surface (*i.e.*, a "hollow" body). Here, we considered the aforementioned (translation-covariant) tensor $W_1^{2,0}$ as well as two other (translation-invariant) Minkowski tensors, namely $W_1^{0,2}$ and $W_2^{0,2}$. The tensor $W_1^{0,2}$ describes the distribution of the surface normal vectors, while $W_2^{0,2}$ describes the distribution of the mean curvature (surface normals weighted by curvature).

Every MT can be used to quantify anisotropy with respect to that particular tensor. We define the degree of anisotropy (DA) for a tensor $W_\nu^{r,s}$ as:

$$DA_\nu^{r,s} = 1 - \frac{\left|\lambda_\nu^{r,s}\right|_{\min}}{\left|\lambda_\nu^{r,s}\right|_{\max}}$$

Here, $|\lambda_\nu^{r,s}|_{\min}$ and $|\lambda_\nu^{r,s}|_{\max}$ are the absolute values of the minimum and maximum eigenvalues of the tensor $W_\nu^{r,s}$. As such, we were able to quantify the different types of anisotropy of the trabecular bone samples, including the anisotropy of the interface orientation ($DA_1^{0,2}$) or the anisotropy of the mean curvature ($DA_2^{0,2}$). For trabecular bone, a classical and popular approach to quantify anisotropy has been based on the mean intercept length (MIL) method [12,38,39]. However, the MIL is limited to interfacial anisotropy (by definition) and is known to suffer from some conceptual shortcomings, such as noise sensitivity, sampling bias, and poor data fitting in specific cases, that could invalidate the anisotropy results [40]. Instead, Minkowski tensors are robust alternatives, showing higher sensitivity to anisotropy in 2D boolean model systems [41]. To assess the potential of Minkowski tensors as alternatives to the MIL tensor for bone anisotropy quantification, we computed the DA of both approaches on 259 trabecular

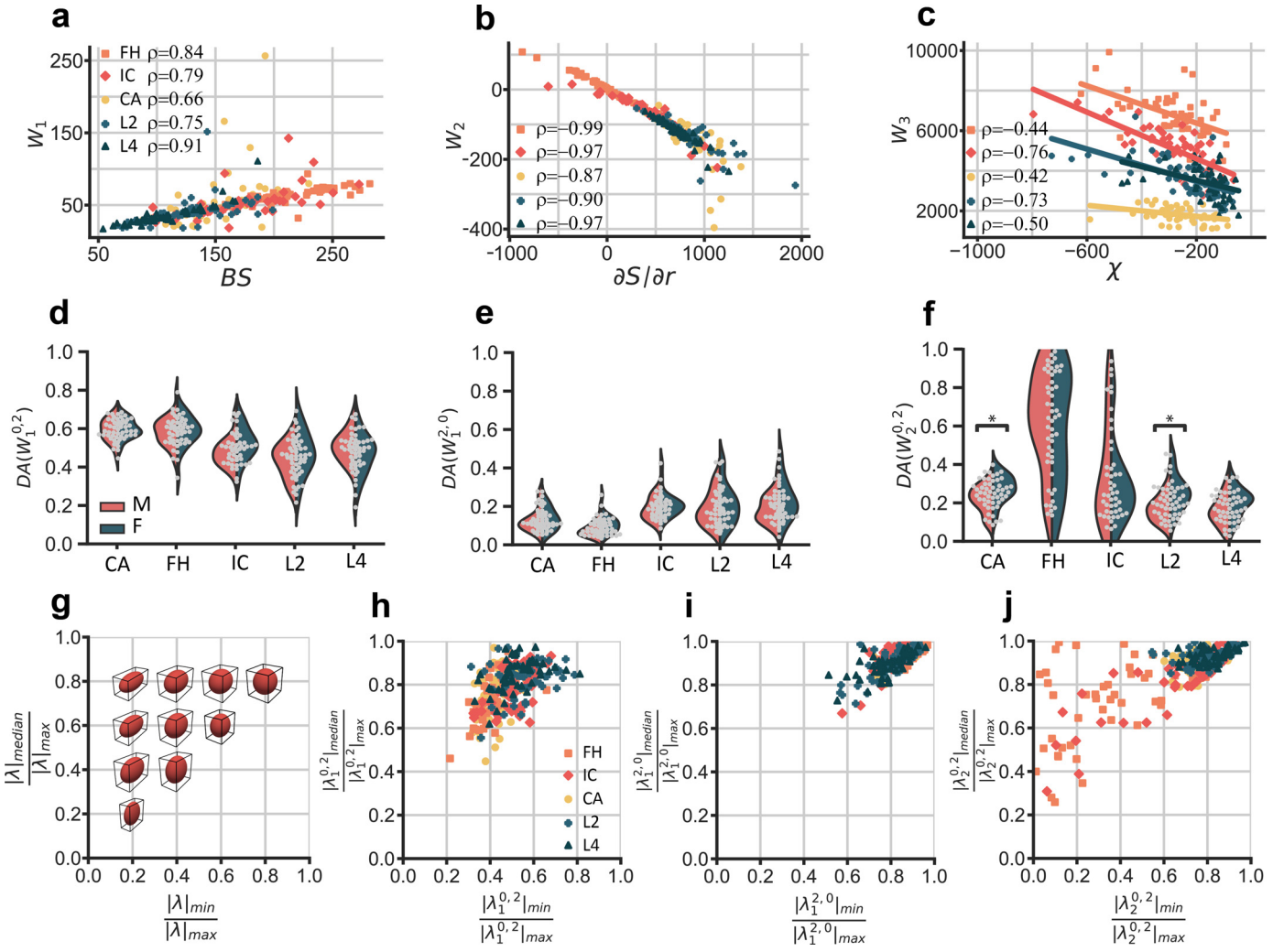

Fig. 9. Scalar and tensorial Minkowski functionals applied to trabecular bone. (a–c) Results for the three Minkowski scalars, plotted *versus* their equivalent standard morphometric index: (a) W_1 *versus* bone surface (BS), (b) W_2 *versus* surface area derivative ($\partial S/\partial r$), (c) W_3 *versus* Euler-Poincaré characteristic (χ). (d–f) The distribution plots for the degree of anisotropy (DA) with respect to the different Minkowski tensors, plotted per anatomical site and split between the specimens from male (M) and female (F) donors: d) DA for tensor $W_1^{0,2}$, e) DA for tensor $W_1^{2,0}$, and f) DA for tensor $W_2^{0,2}$. *: $p<0.01$. g-j) Ellipticity with respect to the different Minkowski tensors, shown as the ratio of the median to the maximum eigenvalue *versus* the ratio of the minimum to the maximum eigenvalue: (g) an illustration of the various degrees of ellipticity, (h) ellipticity with respect to $W_1^{0,2}$, (i) ellipticity with respect to $W_1^{2,0}$, and (j) ellipticity with respect to $W_2^{0,2}$.

bone specimens. The relevant Minkowski tensor for this comparison is $W_1^{0,2}$, as it describes the interfacial orientation. We found that, with the most recent algorithm for the calculation of DA_{MIL} (in BoneJ [42]), all the data for DA_{MIL} and $DA_1^{0,2}$ were strongly correlated (Spearman's $\rho = 0.957$, Pearson's $\rho = 0.963$) and centered around the identity line (Supplementary Fig. 4). Both methods also predicted similar principal directions with most angle differences below 10° (Supplementary Fig. 4b). While theoretical predictions on 2D model systems have indicated that the MIL approach can fail to detect clear anisotropies in certain cases, our analysis indicates that both approaches yield similar results on high-resolution trabecular bone scans [41]. Despite these similar results for our data set, it must be emphasized that DA_{MIL} is highly dependent on the specific MIL implementation, which has been shown to be a potential source of significant variation in classical MIL algorithms [15,43,44]. Moreover, the MT approach is inherently less sensitive to noise as it relies on surface and volume integrals (implying that the contributions of surface roughness are canceled out in the overall computation), while the MIL approach relies on the intersections of test lines with the bone interface (which can be strongly affected by the surface roughness). Additionally, reliable MIL analyses require several runs of the algorithm (due to its stochastic nature), and its algorithmic complexity (computation time) is of the order $\mathcal{O}(N_p \cdot N_l)$ where N_p is the number of pixels and N_l is the number of test lines. The complexity of the MT approach, on the other hand, is only of the order $\mathcal{O}(N_p)$. Finally, the MT approach enables more than one measure of anisotropy, while the MIL is limited to interfacial anisotropy. For a detailed comparison and a theoretical account of both metrics, the reader is referred to a recent study by Klatt et al. [41].

Comparing the $DA_1^{0,2}$ distributions (Fig. 9d), we observed that all bone types exhibit a distinct level of interfacial anisotropy, with significant differences between the means of the different bone types (Supplementary Table 1). Higher mean values were obtained in the CA ($\langle DA_1^{0,2}\rangle = 0.59$) and FH ($\langle DA_1^{0,2}\rangle = 0.58$) specimens, as opposed to the IC ($\langle DA_1^{0,2}\rangle = 0.49$), the L2 ($\langle DA_1^{0,2}\rangle = 0.45$), and L4 ($\langle DA_1^{0,2}\rangle = 0.48$) samples. Moreover, a wider spread in the anisotropy values was observed in the L2 and L4 specimens. In all cases, the degree of anisotropy with respect to the tensor $W_1^{2,0}$, which characterizes the mass distribution of the "hollow" trabecular bone, was much lower (Fig. 9e). Significant differences between the different bone types were detected, and higher mean values

were attained for the IC ($\langle DA_1^{2,0}\rangle$) = 0.20), the L2 ($\langle DA_1^{2,0}\rangle = 0.20$) and the L4 ($\langle DA_1^{2,0} = 0.21$) samples as opposed to the CA ($\langle DA_1^{2,0}\rangle =$ 0.13) and the FH ($\langle DA_1^{2,0} = 0.09$) samples. Finally, $DA_2^{0,2}$ quantifies the anisotropy of the curvature-weighted surface normals (Fig. 5f), again displaying significant differences in the means between the bone types. The CA ($\langle DA_2^{0,2}\rangle = 0.25$), L2 ($\langle DA_2^{0,2}\rangle = 0.21$), and L4 ($\langle DA_2^{0,2}\rangle = 0.18$) specimens exhibited narrower distributions than the FH ($\langle DA_2^{0,2}\rangle = 0.61$) and IC ($\langle DA_2^{0,2}\rangle = 0.33$) specimens. Interestingly, there were statistically significant differences between the mean $DA_2^{0,2}$ values calculated for the specimens harvested from male and female donors in the case of the CA ($n_1 = 25$, $n_2 = 27$, Mann-Withney $U = 179$, p = 0.004) and L2 ($n_1 = 25$, $n_2 = 30$, Mann-Whitney $U = 179$, p = 0.001) bone types.

In reporting DA, only the extremal tensor eigenvalues were considered. To extend our characterization of the Minkowski tensors, we also plotted the ratio of the median to the maximum eigenvalue against the ratio of the minimum to the maximum eigenvalue. Since rank-2 tensors can be represented by the surface of an ellipsoid (Materials & Methods), these plots provide insight into the "ellipticity" of the bone specimens with respect to a particular tensor (Fig. 9g). Data for which $\frac{\lambda_{median}}{\lambda_{max}} = 1$ are represented by prolate spheroids, while data on $\frac{\lambda_{min}}{\lambda_{max}} = \frac{\lambda_{median}}{\lambda_{max}}$ are represented by oblate spheroids. When $\frac{\lambda_{min}}{\lambda_{max}} = \frac{\lambda_{median}}{\lambda_{max}} = 1$, a perfect sphere is obtained and the data is considered fully isotropic with respect to that particular tensor. For the tensor $W_1^{0,2}$, the data was clustered between the oblate and prolate shapes on the ellipsoid spectrum (Fig. 9h). Moreover, the ellipticity of the $W_1^{0,2}$ data was in good agreement with the ellipticity of the MIL data (Supplementary Fig. 4d). In the case of the $W_1^{2,0}$ tensor, most of the specimens were highly concentrated in the nearly isotropic region, with some data points (IC, L2, and L4) exhibiting higher ellipticity (Fig. 5i). For the $W_2^{0,2}$ tensor, the data for the CA, L2 and L4 specimens was again concentrated in the nearly isotropic region, but the data for the FH and IC specimens were scattered over the entire ellipsoid spectrum. For example, the FH specimens covered both highly oblate and prolate ellipticity, with various degrees of anisotropy (Fig. 5j). Taken together, these plots underscore that interfacial orientation is only one of several sources of bone anisotropy and ellipticity, and that other sources can be quantified by considering a different Minkowski tensor (*e.g.* $W_1^{2,0}$ or $W_2^{0,2}$).

3.6. Age-dependency of Minkowski functionals

We plotted the Minkowski scalars (Fig. 10a–c) and the various Minkowski tensor DA's (Fig. 10d–f) *vs.* donor age, for the trabecular bone from the femoral head and the fourth lumbar vertebra, in order to assess whether these metrics could detect age-related changes in the global bone geometry. LOWESS fits were included to aid in visualizing the trends of the data points, similarly to a previous study on age-related bone changes [30]. For both anatomical sites, the Spearman's correlation coefficient (ρ) was computed on the data points of male and female donors separately, as well as on the combination of those data points (Supplementary Tables 2 and 3).

We observed statistically significant and weak to moderate correlations in some of the data sets. Specifically, we found negative correlations in the combined (male and female) L4 data between the age and W_1 ($\rho = -0.51$, $p = 0.0001$), and between the age and W_3 ($\rho = -0.42$, $p = 0.002$). In addition, positive correlations were observed in the male L4 data between the age and $DA_1^{0,2}$ ($\rho = 0.43$, $p = 0.021$), and between the age and $DA_1^{2,0}$ ($\rho = 0.37$, $p = 0.047$). Finally, a weak negative correlation was found in the combined FH data between $DA_2^{0,2}$ and age ($\rho = -0.33$, $p = 0.021$). The fact that these correlations are primarily detected in the L4 specimens confirms the earlier observations that bone from the vertebrae seems to exhibit more pronounced age-related structural changes than bone from the femoral head. Nevertheless, our analysis shows that the correlations are relatively weak, in part due to the large individual variations at advanced age, making it challenging to use these (and other) global metrics to robustly detect age-related changes (*e.g.,* within the context of osteoporosis). However, even more localized analyses have struggled to detect clear age-related trends [30], underscoring the inherent difficulty of capturing the complex morphological changes in aging trabecular bone using single metrics.

3.7. Anisotropy in spatially decomposed bone

The Minkowski functionals provide a global (integral) interpretation of trabecular shape, by assigning either a scalar or a tensor to the entire region of interest. However, the shape and size of this region could be chosen arbitrarily within the cubic specimen volume. Hence, it is possible to apply the Minkowski analysis to several smaller substructures, in order to create a Minkowski map that quantifies the intra-specimen variations of the integral shape indices [2]. In that sense, such a spatially decomposed analysis of the Minkowski functionals occupies an intermediate position between the highly localized analysis of curvature distributions and the whole-specimen shape characterization presented in Sections 3.2. and 3.4.

To quantify the intra-specimen anisotropy changes, we decomposed 100 trabecular specimens into a set of smaller components. In order to maintain representative trabecular substructures, we used a 3 × 3 × 3 cubic grid for this spatial subdivision (Supplementary Fig. 10b). We computed the two translation-invariant Minkowski tensors $W_1^{0,2}$ and $W_2^{0,2}$ on the resulting 2700 substructures, enabling a local characterization of the ellipticity with respect to those tensors. We found that, in general, the ellipticity varies throughout the specimens and is different for both tensors (Fig. 6a–d). To quantify the spatial variation, we calculated the relative difference between the anisotropy of a substructure and that of the entire specimens ($\tilde{\lambda}_v^{r,s}$, Materials & Methods), as well as the angle difference between the local and global principal orientations ($\bar{V}_v^{r,s}$). For both tensors, the local DA varied substantially with respect to the whole-sample value and led to different distributions for both tensors (Fig. 6e). Distinct angle differences in the local and global principal directions were also observed for both tensors, and wider variations were detected in the L2 and L4 specimens (Fig. 6f).

Finally, we asked whether higher-rank Minkowski tensors (beyond rank two) could provide additional insight into the structural and anisotropy differences between the different bone types. To this end, we calculated the quadratic (q_s) and cubic (w_s) rotational invariants of the so-called irreducible Minkowski tensors (Supplementary Note 1) for the spatially decomposed specimens. This analysis was motivated by the recent results in particulate matter, where these scalar invariants have been used as efficient structure metrics to detect local crystalline states in disordered packings of convex shapes [45,46]. Due to their higher-rank nature, however, the physical significance of these structure metrics is less easily understood than for the rank-2 Minkowski tensors. Plotting the probability distributions of q_s and w_s for the FH and L4 specimens (540 data points each, Supplementary Figs. 5 and 6), we observed globally smooth distributions for q_s and w_s that are qualitatively similar to those obtained for hyperuniform amorphous cellular solids [46]. Sharp peaks in the distribution would indicate the presence of a locally crystalline region with a certain structural symmetry. Significant differences between the structure metric distributions of the FH and L4 specimens were detected (two-sample Kolmogorov-Smirnov, $p < 0.01$), except for q_5, indicating that these

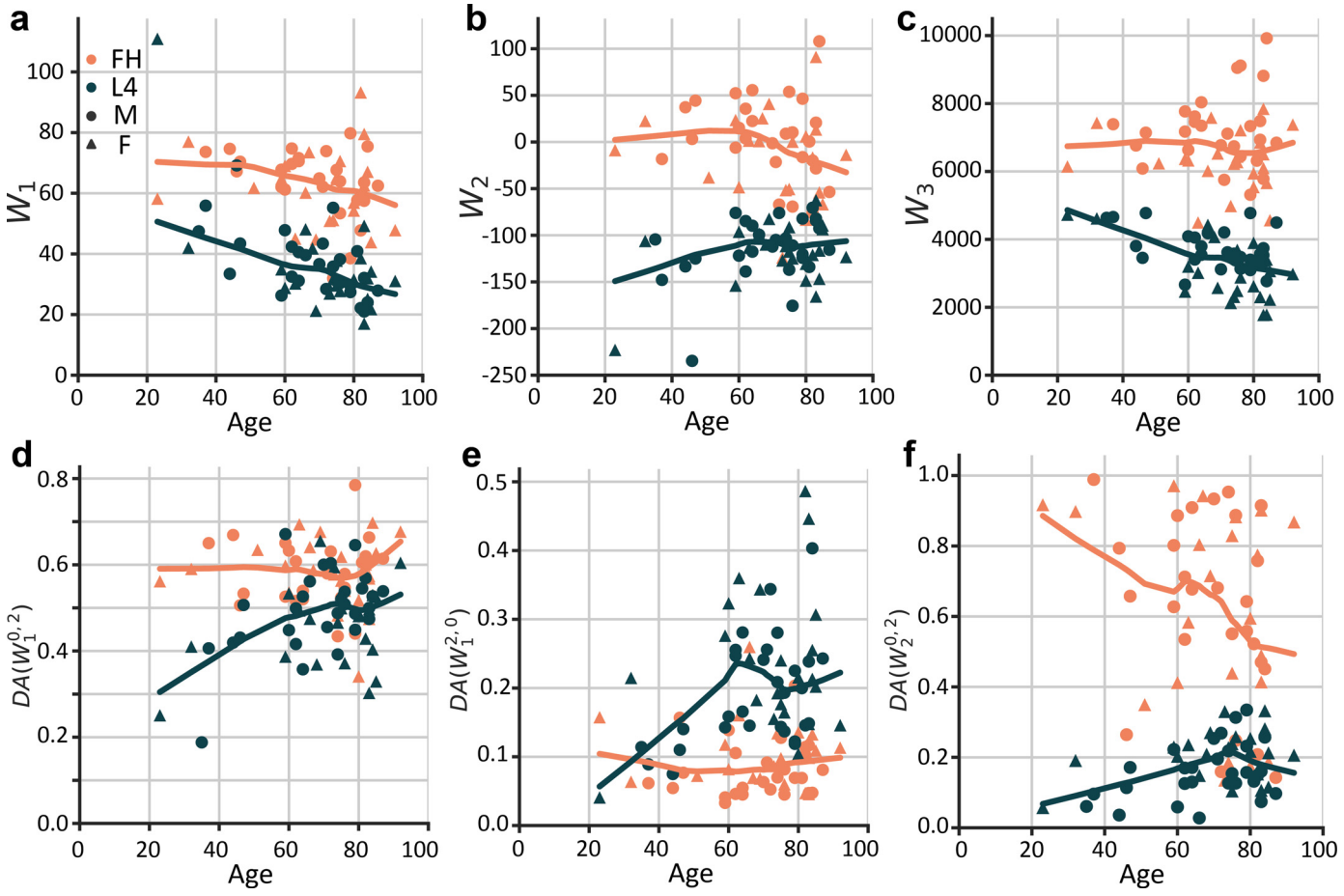

Fig. 10. Scalar and tensorial Minkowski functionals for FH and L4 *vs* age. (a–c) Results for the three Minkowski scalars, plotted *vs.* age. The circular and triangular data points correspond to the specimens from male and female donors, respectively.(d–f) The DA for the three Minkowski tensors, plotted *vs.* age. The curves are LOWESS fits through the corresponding data points.

higher-order structure metrics are sensitive to the structural differences between the plate-like and rod-like specimens (Fig. 11).

4. Discussion

The aim of this study was to provide a more fundamental geometric viewpoint on the quantification of trabecular bone shape. Such a geometry-centered approach not only offers a more mathematical foundation to the longstanding field of trabecular bone morphometry, but also provides a framework to study other spatially complex materials, including bone-mimicking architected scaffolds and biomaterials (*e.g.* metabiomaterials [47]). At the local perspective, this geometric characterization could be accomplished by quantifying the surface curvature of the trabecular interface. In fact, curvature is the defining characteristic when it comes to distinguishing between local structural features, such as rods ($K = 0$, $H < 0$), plates ($K = 0$, $H = 0$), and saddle-shaped arcs ($K < 0$), or to identify primarily convex ($H < 0$) or concave ($H > 0$) regions. We quantified the complex curved landscapes of trabecular bone using the ISD, finding that these density maps serve as effective shape fingerprints for trabecular bone from different anatomical sites. Indeed, the ISD captured the morphological differences between so-called plate-like (FH) and rod-like (L2 and L4) specimens, but were also sensitive to intermediate morphologies along the plate-rod spectrum (IC and CA). In fact, the ISD analysis demonstrated that the morphology of trabecular bone is much more complex, containing many local shape variations, than what is implied when using the qualitative descriptions of plate-like and rod-like samples [48]. Additionally, earlier attempts at quantifying this plate-like or rod-like behavior were based on the SMI, which does not capture all possible shapes (Fig. 4b) [14]. Furthermore, we found that the surface curvature distributions of the bone from the lumbar vertebrae showed age-dependencies, and that surface curvatures could be good descriptors of local changes in age-related bone adaptions, such as perforations and rod thinning (*e.g.*, for simulated bone atrophy [49]).

Due to the generality of studying surface curvature distributions, this type of analysis could easily be extended to quantify the interface of other geometrically and topologically complex morphologies, such as those of porous bone scaffolds. As a demonstration, we applied the curvature analysis to $3 \times 3 \times 3$ lattices of the octet truss and gyroid minimal surface, as well as a stochastic "spinodoid" [50] based on a Gaussian random field (GRF, Fig. 12). The principal curvature ISD of the octet truss demonstrated the limited curvature spectrum, containing primarily cylindrical elements and only exhibiting non-zero Gaussian curvature at the strut intersections. The gyroid minimal surface, which has often been claimed to be a "bone-mimicking" morphology, is characterized by a vanishing mean curvature and a negative (or zero) Gaussian curvature along the surface, resulting in a very narrow ISD spectrum. However, the stochastic GRF scaffold shows a broader curvature spectrum that more closely approximates that of trabecular bone, especially of the FH specimens. However, this ISD is symmetric around the line $\kappa_1 = -\kappa_2$, which was not observed in any of the bone specimens. While this type of analysis could be applied to assess the "bone-mimicking" nature of various scaffold morpholo-

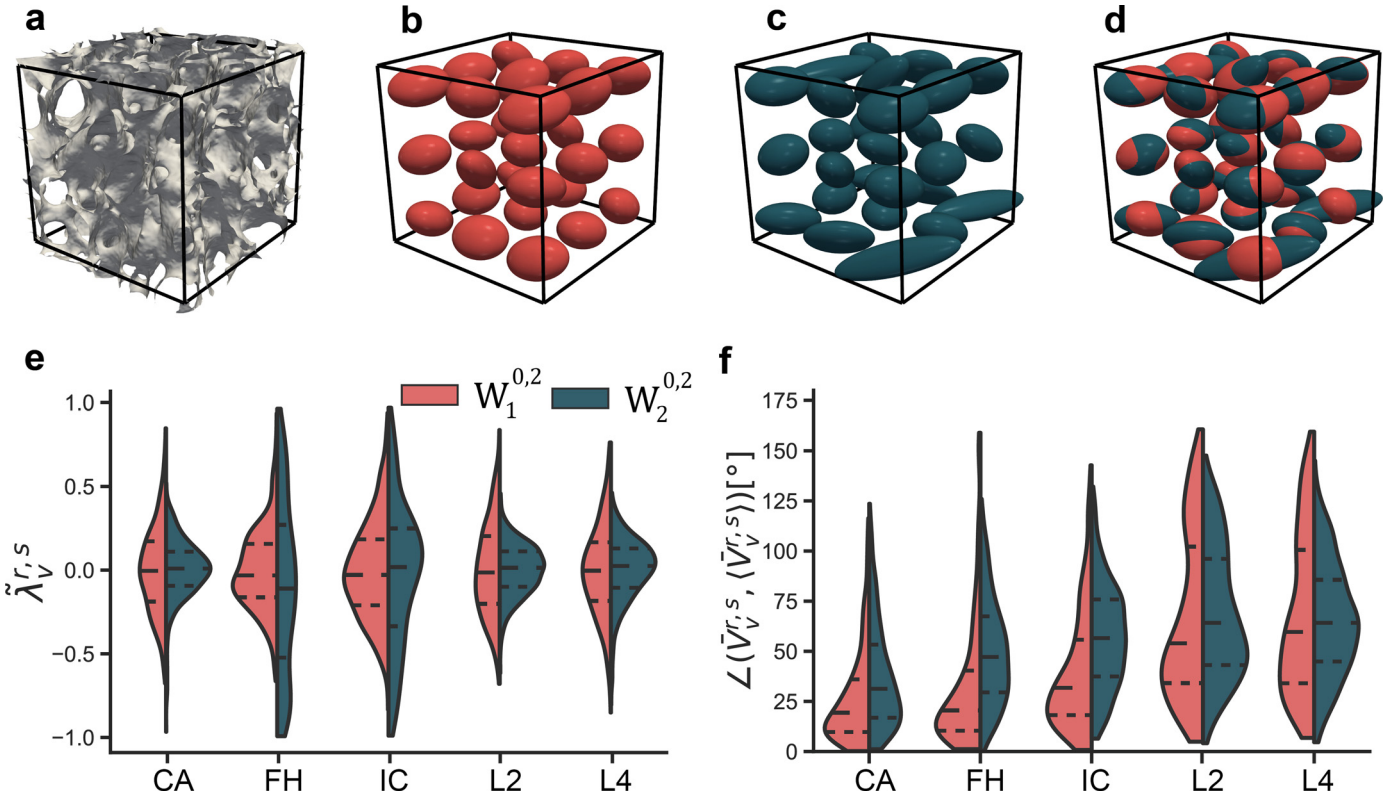

Fig. 11. Minkowski tensor analysis on spatially decomposed samples. (a) A visualization of a full FH trabecular bone specimen. (b) Ellipticity with respect to the normal density tensor ($W_1^{0,2}$) of the sample in (a) in 27 subdomains. The ellipsoids are oriented in their principal direction. (c) Ellipticity with respect to the curvature density tensor ($W_2^{0,2}$) of the sample in a) at 27 subdomains. (d) An overlay of the ellipticities of (b and c). (e) The relative differences in the local and global anisotropy for $W_1^{0,2}$ and $W_2^{0,2}$, plotted for each anatomical site. (f) The differences in the local and global principal orientations for $W_1^{0,2}$ and $W_2^{0,2}$, plotted for each anatomical site.

gies, it should be noted that a bone-matching ISD does not necessarily imply successful scaffold functionality, since this would depend upon a myriad of mechanical, mass transport, and biological requirements [51].

We also performed a global shape analysis of the trabecular bone interface. To this end, we employed the scalar and tensorial Minkowski functionals, since these are fundamental, highly versatile, and robust indices for integral shape quantification. We found that the Minkowski scalars, which were computed directly on the triangulated bone meshes, correlated with traditional bone morphometric indices, such as BS, $\partial S/\partial r$, or χ. Moreover, we found that W_3 was more sensitive to differences in bone microarchitecture than the corresponding traditional metric χ. Our work was the first to apply the Minkowski tensors to the quantification of trabecular bone shape. This analysis revealed different degrees of anisotropy and ellipticity, depending on the morphological aspect that is being considered. Moreover, anisotropy differences between bone specimens harvested from different anatomical sites could be detected. An important aspect of this Minkowski functional approach is that it unifies several traditional morphometric indices within the same geometrical theory. For example, interfacial and volume anisotropy are traditionally characterized using different methods (*e.g.,* the MIL and SVD methods), while both can be described within the Minkowski tensor framework by using a different tensor. We investigated changes in the Minkowski scalars and tensors with age, and detected moderate (significant) correlations in some datasets, particularly those pertaining to the vertebrae. However, large variations between individuals make it difficult to detect age-related changes using global metrics, and more detailed investigations would be required to assess whether some of these Minkowski metrics could serve as robust detectors of age-related changes. We also applied higher-rank Minkowski metrics to the shape quantification of spatially-decomposed bone specimens, showing that they are also sensitive to morphological differences in bone from different anatomical sites. However, we note that these higher-rank metrics are usually applied to disordered assemblies of discrete convex bodies, such as the Voronoi diagram of a granular packing [45,46]. Such materials are naturally well-suited for this type of domain-wise analysis, since the basic definition of these structure metrics is centered around decomposing the normal density of convex bodies into spherical harmonics. As such, analyses using these metrics might be more compatible with convex particle systems than with non-convex, smooth trabecular bone structures. In this regard, it would be interesting to apply this analysis to specimens that are decomposed into (almost) convex units, for example by volumetric decomposition into rods and plates [34], or by approximate convex decomposition [52]. Additionally, the use of clustering algorithms (*e.g.* k-means or DBSCAN) could shed light on the classification sensitivity of such higher-order metrics.

The key characteristic of our metrics is their fundamental geometric nature, which offers a unifying view and geometrical foundation for traditional bone morphometric indices. This geometric perspective could advance the understanding of morphological changes in aging and disease, such as the elusive plate-to-rod transition in osteoporosis [48]. Our approaches could also provide a framework for shape description within the context of bone healing, for example, to characterize the structure of the developing callus *in vivo* [53,54]. Since these metrics are not bound by scale, they could also readily be applied to high-resolution images of much smaller structures within bone, such as the lacuno-canalicular network [55]. Moreover, our insights into trabecular

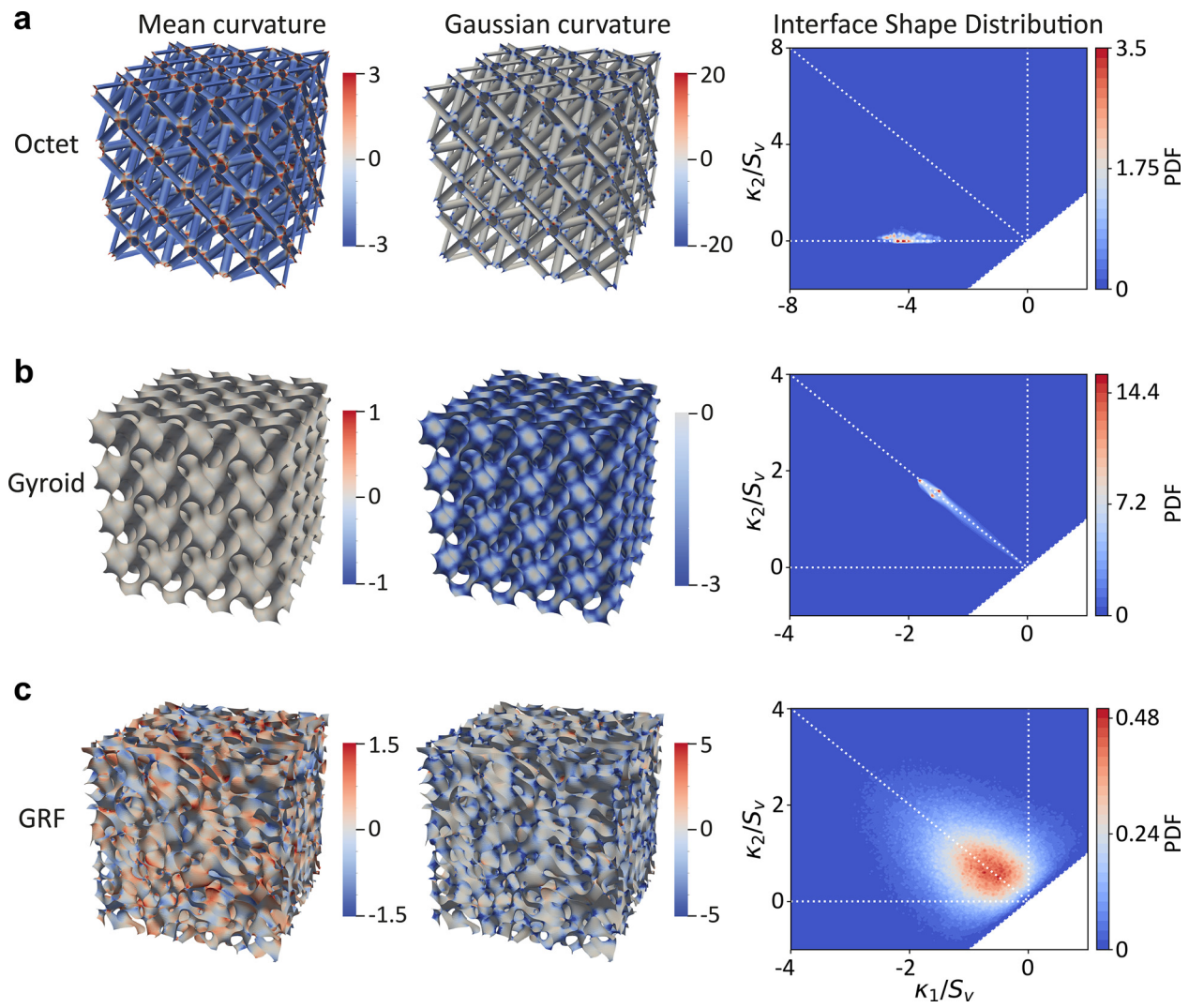

Fig. 12. Curvature visualizations and ISD for several scaffold morphologies. The left column displays the normalized mean curvature, the middle column displays the normalized Gaussian curvature, and the right column displays the principal curvature ISD. (a) The interface of the octet truss lattice. (b) The interface of a gyroid minimal surface lattice. (c) The interface of a stochastic lattice based on a Gaussian random field (GRF).

bone curvature are relevant for recent investigations into the role of substrate curvature as a mechanobiological cue at the cell and tissue levels [7,56], which could be leveraged in tissue engineering applications. Finally, it would be interesting to couple these geometrical analyses to mechanics-driven bone simulation frameworks, for example, to investigate whether this type of geometric data could provide additional insights for bone remodeling algorithms or fracture predictions.

5. Conclusion

In summary, we have provided a geometric approach to trabecular bone morphometry, quantifying both the local and global shape of trabecular bone, and unifying several traditional morphometric indices within the mathematical language of geometry. Our analyses were centered around surface curvature and Minkowski functionals, which proved to be sensitive fingerprints to site-specific differences in bone morphology. These approaches could facilitate the geometrical characterization of a broad spectrum of spatially-complex materials beyond bone, ultimately advancing the development of accurate structure-property relationships for such materials.

Declaration of Competing Interest

The authors declare that they have no known competing financial interests or personal relationships that could have appeared to influence the work reported in this paper.

Acknowledgments

The first author is thankful to Dr. Fabian Schaller and Dr. Sebastian Kapfer for sharing insights on the use and interpretation of the Karambola software, which was used for the computation of the Minkowski functionals, to Prof. Amber Genau and Dr. Delphine De Tavernier for useful discussions on the implementation of the radial distribution functions, and to the IDEA League program for facilitating an exchange at ETH Zurich. The research leading to these results has received funding from the European Research Council under the ERC grant agreements no. [677575] and [741883].

Supplementary materials

Supplementary material associated with this article can be found, in the online version, at doi:10.1016/j.actbio.2021.06.013.

References

[1] U.G. Wegst, H. Bai, E. Saiz, A.P. Tomsia, R.O. Ritchie, Bioinspired structural materials, Nat. Mater. 14 (1) (2015) 23–36.
[2] G.E. Schröder-Turk, W. Mickel, S.C. Kapfer, M.A. Klatt, F.M. Schaller, M.J.F. Hoffmann, N. Kleppmann, P. Armstrong, A. Inayat, D. Hug, M. Reichelsdorfer, W. Peukert, W. Schwieger, K. Mecke, Minkowski tensor shape analysis of cellular, granular and porous structures, Adv. Mater. 23 (22–23) (2011) 2535–2553.
[3] R. Huiskes, R. Ruimerman, G.H. Van Lenthe, J.D. Janssen, Effects of mechanical forces on maintenance and adaptation of form in trabecular bone, Nature 405 (6787) (2000) 704–706.
[4] A. Parfitt, C. Mathews, A. Villanueva, M. Kleerekoper, B. Frame, D. Rao, Relationships between surface, volume, and thickness of iliac trabecular bone in aging and in osteoporosis. Implications for the microanatomic and cellular mechanisms of bone loss, J. Clin. Investig. 72 (4) (1983) 1396–1409.
[5] T. Hildebrand, A. Laib, R. Müller, J. Dequeker, P. Rüegsegger, Direct three-dimensional morphometric analysis of human cancellous bone: microstructural data from spine, femur, iliac crest, and calcaneus, J. Bone Miner. Res. 14 (7) (1999) 1167–1174.
[6] A.A. Zadpoor, Mechanical meta-materials, Mater. Horiz. 3 (5) (2016) 371–381.
[7] S.J. Callens, R.J. Uyttendaele, L.E. Fratila-Apachitei, A.A. Zadpoor, Substrate curvature as a cue to guide spatiotemporal cell and tissue organization, Biomaterials 232 (2020) 119739.
[8] M. Rumpler, A. Woesz, J.W. Dunlop, J.T. van Dongen, P. Fratzl, The effect of geometry on three-dimensional tissue growth, J. R. Soc. Interface 5 (27) (2008) 1173–1180.
[9] L. Pieuchot, J. Marteau, A. Guignandon, T. Dos Santos, I. Brigaud, P.-F. Chauvy, T. Cloatre, A. Ponche, T. Petithory, P. Rougerie, M. Vassaux, J.L. Milan, N.T. Wakhloo, A. Spangenberg, M. Bigerelle, K. Anselme, Curvotaxis directs cell migration through cell-scale curvature landscapes, Nat. Commun. 9 (1) (2018) 3995.
[10] S. Ehrig, B. Schamberger, C. Bidan, A. West, C. Jacobi, K. Lam, P. Kollmannsberger, A. Petersen, P. Tomancak, K. Kommareddy, Surface tension determines tissue shape and growth kinetics, Sci. Adv. 5 (9) (2019) eaav9394.
[11] M.L. Bouxsein, S.K. Boyd, B.A. Christiansen, R.E. Guldberg, K.J. Jepsen, R. Müller, Guidelines for assessment of bone microstructure in rodents using micro–computed tomography, J. Bone Miner. Res. 25 (7) (2010) 1468–1486.
[12] A. Odgaard, Three-dimensional methods for quantification of cancellous bone architecture, Bone 20 (4) (1997) 315–328.
[13] T. Hildebrand, P. Rüegsegger, Quantification of bone microarchitecture with the structure model index, Comput. Methods Biomech. Biomed. Eng. 1 (1) (1997) 15–23.
[14] P.L. Salmon, C. Ohlsson, S.J. Shefelbine, M. Doube, Structure model index does not measure rods and plates in trabecular bone, Front. Endocrinol. 6 (2015) 162 (Lausanne).
[15] L. Steiner, A. Synek, D.H. Pahr, Comparison of different microCT-based morphology assessment tools using human trabecular bone, Bone Rep. 12 (2020) 100261.
[16] K. Verdelis, L. Lukashova, E. Atti, P. Mayer-Kuckuk, M. Peterson, S. Tetradis, A. Boskey, M. van der Meulen, MicroCT morphometry analysis of mouse cancellous bone: intra-and inter-system reproducibility, Bone 49 (3) (2011) 580–587.
[17] S.C. Kapfer, W. Mickel, K. Mecke, G.E. Schröder-Turk, Jammed spheres: minkowski tensors reveal onset of local crystallinity, Phys. Rev. E 85 (3) (2012) 030301.
[18] F.M. Schaller, S.C. Kapfer, J.E. Hilton, P.W. Cleary, K. Mecke, C. De Michele, T. Schilling, M. Saadatfar, M. Schröter, G.W. Delaney, Non-universal Voronoi cell shapes in amorphous ellipsoid packs, EPL (Europhys. Lett.) 111 (2) (2015) 24002.
[19] S. Alesker, Description of continuous isometry covariant valuations on convex sets, Geom. Dedicata 74 (3) (1999) 241–248.
[20] G.E. Schröder-Turk, W. Mickel, S.C. Kapfer, F.M. Schaller, B. Breidenbach, D. Hug, K. Mecke, Minkowski tensors of anisotropic spatial structure, New J. Phys. 15 (8) (2013) 083028.
[21] H. Hadwiger, Vorlesungen über Inhalt, Oberfläche und Isoperimetrie, Springer-Verlag, 2013.
[22] A. Genau, P. Voorhees, K. Thornton, The morphology of topologically complex interfaces, Scr. Mater. 60 (5) (2009) 301–304.
[23] S.C. Cowin, The relationship between the elasticity tensor and the fabric tensor, Mech. Mater. 4 (2) (1985) 137–147.
[24] A. Odgaard, J. Kabel, B. van Rietbergen, M. Dalstra, R. Huiskes, Fabric and elastic principal directions of cancellous bone are closely related, J. Biomech. 30 (5) (1997) 487–495.
[25] S. Hyde, Z. Blum, T. Landh, S. Lidin, B.W. Ninham, S. Andersson, K. Larsson, The Language of Shape: The Role of Curvature in Condensed Matter: Physics, Chemistry and Biology, Elsevier Science, Amsterdam, the Netherlands, 1996.
[26] H. Jinnai, H. Watashiba, T. Kajihara, Y. Nishikawa, M. Takahashi, M. Ito, Surface curvatures of trabecular bone microarchitecture, Bone 30 (1) (2002) 191–194.
[27] D. Hilbert, S. Cohn-Vossen, Geometry and The Imagination, Chelsea Publishing Company, New York, USA, 1990.
[28] C.-L. Park, J. Gibbs, P.W. Voorhees, K. Thornton, Coarsening of complex microstructures following spinodal decomposition, Acta Mater. 132 (2017) 13–24.
[29] R. Mendoza, I. Savin, K. Thornton, P.W. Voorhees, Topological complexity and the dynamics of coarsening, Nat. Mater. 3 (6) (2004) 385–388.
[30] M. Stauber, R. Muller, Age-related changes in trabecular bone microstructures: global and local morphometry, Osteoporos. Int. 17 (4) (2006) 616–626.
[31] N. Akaiwa, P.W. Voorhees, Late-stage phase separation: dynamics, spatial correlations, and structure functions, Phys. Rev. E 49 (5) (1994) 3860.
[32] A. Genau, P.W. Voorhees, Spatial correlations in symmetric and asymmetric bicontinuous structures, Acta Mater. 57 (20) (2009) 6226–6233.
[33] C. Räth, R. Monetti, J. Bauer, I. Sidorenko, D. Müller, M. Matsuura, E. Lochmüller, P. Zysset, F. Eckstein, Strength through structure: visualization and local assessment of the trabecular bone structure, New J. Phys. 10 (12) (2008) 125010.
[34] M. Stauber, R. Müller, Volumetric spatial decomposition of trabecular bone into rods and plates-a new method for local bone morphometry, Bone 38 (4) (2006) 475–484.
[35] M. Hahn, M. Vogel, M. Pompesius-Kempa, G. Delling, Trabecular bone pattern factor-a new parameter for simple quantification of bone microarchitecture, Bone 13 (4) (1992) 327–330.
[36] M. Saadatfar, M. Mukherjee, M. Madadi, G. Schröder-Turk, F. Garcia-Moreno, F. Schaller, S. Hutzler, A. Sheppard, J. Banhart, U. Ramamurty, Structure and deformation correlation of closed-cell aluminium foam subject to uniaxial compression, Acta Mater. 60 (8) (2012) 3604–3615.
[37] C. Beisbart, R. Dahlke, K. Mecke, H. Wagner, Vector-and tensor-valued descriptors for spatial patterns, in: Morphology of Condensed Matter, Springer, 2002, pp. 238–260.
[38] T. Harrigan, R. Mann, Characterization of microstructural anisotropy in orthotropic materials using a second rank tensor, J. Mater. Sci. 19 (3) (1984) 761–767.
[39] W. Whitehouse, The quantitative morphology of anisotropic trabecular bone, J. Microsc. 101 (2) (1974) 153–168.
[40] M.A. Klatt, G.E. Schröder-Turk, K. Mecke, Mean-intercept anisotropy analysis of porous media. I. analytic formulae for anisotropic Boolean models, Med. Phys. 44 (7) (2017) 3650–3662.
[41] M.A. Klatt, G.E. Schröder-Turk, K. Mecke, Mean-intercept anisotropy analysis of porous media. II. Conceptual shortcomings of the MIL tensor definition and Minkowski tensors as an alternative, Med. Phys. 44 (7) (2017) 3663–3675.
[42] M. Doube, M.M. Kłosowski, I. Arganda-Carreras, F.P. Cordelières, R.P. Dougherty, J.S. Jackson, B. Schmid, J.R. Hutchinson, S.J. Shefelbine, BoneJ: free and extensible bone image analysis in ImageJ, Bone 47 (6) (2010) 1076–1079.
[43] C.A. Simmons, J.A. Hipp, Method-based differences in the automated analysis of the three-dimensional morphology of trabecular bone, J. Bone Miner. Res. 12 (6) (1997) 942–947.
[44] R. Ketcham, T.M. Ryan, Quantification and visualization of anisotropy in trabecular bone, J. Microsc. 213 (2) (2004) 158–171.
[45] W. Mickel, S.C. Kapfer, G.E. Schröder-Turk, K. Mecke, Shortcomings of the bond orientational order parameters for the analysis of disordered particulate matter, J. Chem. Phys. 138 (4) (2013) 044501.
[46] M.A. Klatt, J. Lovrić, D. Chen, S.C. Kapfer, F.M. Schaller, P.W. Schönhöfer, B.S. Gardiner, A.S. Smith, G.E. Schröder-Turk, S. Torquato, Universal hidden order in amorphous cellular geometries, Nat. Commun. 10 (1) (2019) 1–9.
[47] A.A. Zadpoor, Meta-biomaterials, Biomater. Sci. 8 (1) (2020) 18–38.
[48] A.A. Felder, S. Monzem, R. De Souza, B. Javaheri, D. Mills, A. Boyde, M. Doube, The plate-to-rod transition in trabecular bone loss is elusive, R. Soc. Open Sci. 8 (2021) 201401, doi:10.1098/rsos.201401.
[49] R. Mueller, W.C. Hayes, Biomechanical competence of microstructural bone in the progress of adaptive bone remodeling, in: Proceedings of the Developments in X-ray Tomography, International Society for Optics and Photonics, 1997, pp. 69–81.
[50] S. Kumar, S. Tan, L. Zheng, D.M. Kochmann, Inverse-designed spinodoid metamaterials, NPJ Comput. Mater. 6 (1) (2020) 1–10.
[51] F.J. O'Brien, Biomaterials \& scaffolds for tissue engineering, Mater. Today 14 (3) (2011) 88–95.
[52] J.M. Lien, N.M. Amato, Approximate convex decomposition of polyhedra, in: Proceedings of the ACM symposium on Solid and Physical Modeling, 2007, pp. 121–131.
[53] E. Wehrle, D.C.T. né Betts, G.A. Kuhn, A.C. Scheuren, S. Hofmann, R. Müller, Evaluation of longitudinal time-lapsed *in vivo* micro-CT for monitoring fracture healing in mouse femur defect models, Sci. Rep. 9 (1) (2019) 1–12.
[54] D.C.T. né Betts, E. Wehrle, G.R. Paul, G.A. Kuhn, P. Christen, S. Hofmann, R. Müller, The association between mineralised tissue formation and the mechanical local *in vivo* environment: time-lapsed quantification of a mouse defect healing model, Sci. Rep. 10 (1) (2020) 1–10.
[55] P. Goggin, K. Zygalakis, R. Oreffo, P. Schneider, High-resolution 3D imaging of osteocytes and computational modelling in mechanobiology: insights on bone development, ageing, health and disease, Eur. Cells Mater. 31 (2016) 264–295.
[56] M. Werner, N.A. Kurniawan, C.V. Bouten, Cellular geometry sensing at different length scales and its implications for scaffold design, Materials 13 (4) (2020) 963 (Basel).
[57] J. Dequeker, Assessment of quality of bone in osteoporosis–BIOMED I: fundamental study of relevant bone, Clin. Rheumatol. 13 (1994) 7–12.
[58] A. Jacobson, D. Panozzo, C. Schüller, O. Diamanti, Q. Zhou, N. Pietroni, libigl: a simple C++ geometry processing library, 2016. http://libigl.github.io/libigl, Last accessed on 17 June 2021.
[59] M. Dawson-Haggerty, Trimesh 3.2.0, 2019. https://trimsh.org, Last accessed on 17 June 2021.
[60] T. Lewiner, H. Lopes, A.W. Vieira, G. Tavares, Efficient implementation of marching cubes' cases with topological guarantees, J. Graph. Tools 8 (2) (2003) 1–15.

[61] M. Desbrun, M. Meyer, P. Schröder, A.H. Barr, Implicit fairing of irregular meshes using diffusion and curvature flow, in: Proceedings of the 26th Annual Conference on Computer Graphics and Interactive Techniques, 1999, pp. 317–324.
[62] D. Panozzo, E. Puppo, L. Rocca, Efficient multi-scale curvature and crease estimation, in: Proceedings of the Computer Graphics, Computer Vision and Mathematics, 1, Brno, Czech Rapubic, 2010.
[63] F. Cazals, M. Pouget, Estimating differential quantities using polynomial fitting of osculating jets, Comput. Aided Geom. Des. 22 (2) (2005) 121–146.
[64] P. Cignoni, M. Callieri, M. Corsini, M. Dellepiane, F. Ganovelli, G. Ranzuglia, Meshlab: an open-source mesh processing tool, in: Proceedings of the Eurographics Italian Chapter Conference, 2008, pp. 129–136.